2

AU-3
3

AUG 12 1993

Coal-Fired High Performance Power Generating System

DE-AC22-92PC91155

Quarterly Progress Report

for the Period January 1 - March 31, 1992

Prepared for

Pittsburgh Energy Technology Center

Pittsburgh, Pennsylvania

United Technologies Research Center

411 Silver Lane, East Hartford, Connecticut 06108

MASTER

DISTRIBUTION OF THIS DOCUMENT IS UNLIMITED

Executive Summary

This report covers work carried out under Task 2, Concept Definition and Analysis, and Task 3, Preliminary R and D, under contract DE-AC22-92PC91155, "Engineering Development of a Coal Fired High Performance Power Generation System" between DOE Pittsburgh Energy Technology Center and United Technologies Research Center.

The goals of the program are to develop a coal-fired high performance power generation system (HIPPS) by the year 2000 that is capable of

- $>47\%$ thermal efficiency
- NO_x, SO_x and Particulates $\leq 25\%$ NSPS
- cost $\geq 65\%$ of heat input
- all solid wastes benign

In order to achieve these goals our team has outlined a research plan based on an optimized analysis of a 250 MW_e combined cycle system applicable to both frame type and aeroderivative gas turbines. Under the constraints of the cycle analysis we have designed a high temperature advanced furnace (HITAF) which integrates several combustor and air heater designs with appropriate ash management procedures.

The cycle optimization effort has brought about several revisions to the system configuration resulting from:

1) the use of Illinois No. 6 coal instead of Utah Blind Canyon; 2) the use of coal rather than methane as a reburn fuel; 3) reducing radiant section outlet temperatures to 1700F (down from 1800F); and 4) the need to use higher performance (higher cost) steam cycles to offset losses introduced as more realistic operating and construction constraints are identified.

Modeling studies on the long-axial-flame have continued, now using the Illinois No. 6 bituminous coal. A preliminary HITAF design based on the combustion model is presented in this report. In addition, some preliminary experimental results have been obtained from the 100,000 BTU/hr facility. The results on NO_x control by fuel staging and reburning will provide the testing ground for modeling studies.

The optimization studies of the radiant air heater have continued. Recent efforts have focused on calculating the slag film history using a temperature dependent slag viscosity. This improvement allows more accurate predictions of the heat transfer in the radiant panel design.

The studies of slag interaction with structural SiC and refractory coatings has continued and some recent results are presented in this report. A preliminary recommendation for the refractory coating of SiC panels is to use a commercial castable or gunnable SiC refractory coating.

The design of the duct heater has been revised as a result of some experimental results indicating that wall-mounted centrifugal mixers would not penetrate to the centerline. The new design has all the mixers located on the bulkhead. Measurements of the mixing rate for conditions of our HIPPS design show complete mixing in 1.1 diameters.

An appendix to this report includes the design criteria for our commercial plant.

TABLE OF CONTENTS

LIST OF FIGURES

LIST OF TABLES

TASK 2.1 CYCLE OPTIMIZATION

Modifications to the HITAF coal combustor and heat exchangers require changes in the baseline cycle described in the previous report. This is an iteration process in which the effects of HITAF variations are evaluated and the performance trends used to guide the next round of HITAF perturbations. Effort continues on adapting the Humid Air Turbine (HAT) cycle based on the Pratt & Whitney advanced aero-derivative FT4000 engine.

Baseline Cycle Revisions

Revisions to the system configuration have resulted from several changes: 1) the use of Illinois No. 6 coal instead of Utah Blind Canyon; 2) the use of coal rather than methane as a reburn fuel; 3) reducing radiant section outlet temperatures to 1700 F (down from 1800 F); and 4) the need to use higher performance (higher cost) steam cycles to off-set losses introduced as more realistic operating and construction constraints are identified.

A revised cycle diagram based on the use of a dried Illinois No. 6 coal is given in Fig. 1. Compared to the previous system (Fig. 2), the major differences are the relocation of the recirculation (quench) air from within the HRSG to a point prior to the FGD. This results in a somewhat decreased heat load in the HRSG and was best matched by an 1800 psi/950 F/950 F steam system.

In previous systems, approximately five percentage points of heat input from the methane fraction (from a total of 35%) has been assumed for use in the HITAF as fuel for re-burn for NOx control. A new version, shown schematically in Fig.3 uses coal fines for this duty, allowing the methane to be used in the duct burner. Doing this allows the outlet temperature of the radiant section to be dropped from 1800F to 1700F, while maintaining the desired methane to coal fraction.

As the HITAF design nears finalization, consideration of the realities of construction and assembly requires a re-examination of several assumptions. For example, the pressure drop of the compressor discharge air in the radiant and convective heater has been underestimated. The previous value of 1.74% has been increased to 2.5%, resulting in a efficiency loss of 0.07 points.

Another change evaluated was the relocation of the recirculating (quench) flow to downstream of the FGD rather than upstream. This would allow the induced draft fan to supply the head for the recirculation flow. This would reduce the temperature of the quench gas from 240F to 115F. The resulting loss in the steam raising capacity of the flow in the HRSG is the difference between the temperature prior to the FGD (240F)and the new temperature of 115F, or about 7350 Btu/sec. This would be equivalent to a net reduction of 2.8 MW in the steam cycle, or a loss in efficiency of 0.41 points. To avoid this loss, a second, small recirculation fan was added to the system.

A seemingly innocuous change was suggested by Bechtel; removing the steam heater for the methane fuel. They were concerned that the heater was small, the pipe run relatively long and that the losses might negate any cycle advantage. The heater supplies only 3000 Btu/sec to the methane out of a total cycle heat of 596,000, Btu/sec, approximately 0.5%. Since the heat previously going to the methane would be recovered for use in the steam cycle at about 35% efficiency rather than at the 50% of the combined cycle, one would anticipate a 0.05% change. However, due to the need to preserve the split between methane and coal (35%/65%) and the difference between HHV and LHV, there are broader results.

FIGURE 1. PRELIMINARY HEAT BALANCE - GT EXHAUST-FIRED
CLEANED ILLINOIS No. 6 DRY

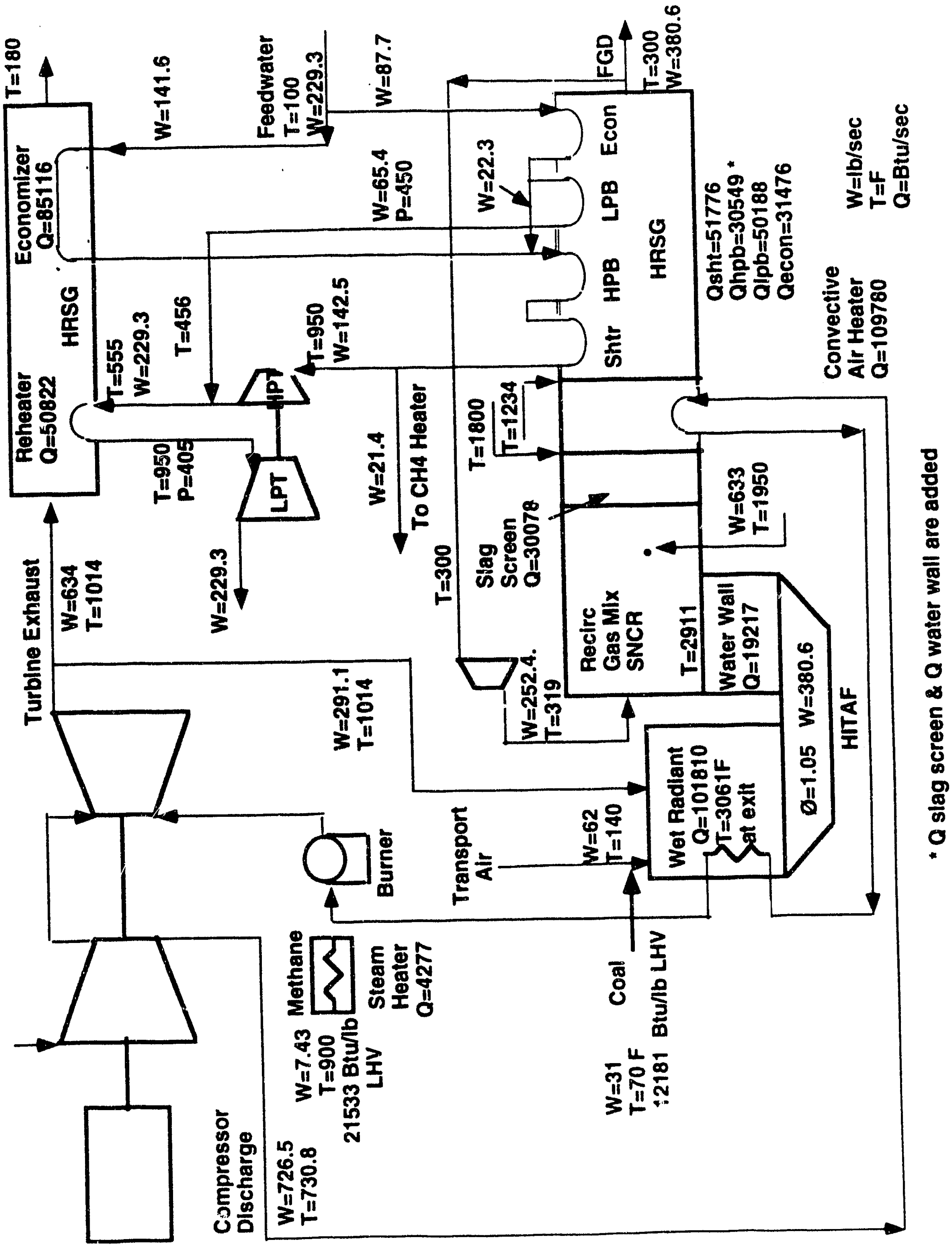

FIGURE 2. PRELIMINARY HEAT BALANCE - GT EXHAUST FIRED
BLIND CANYON COAL

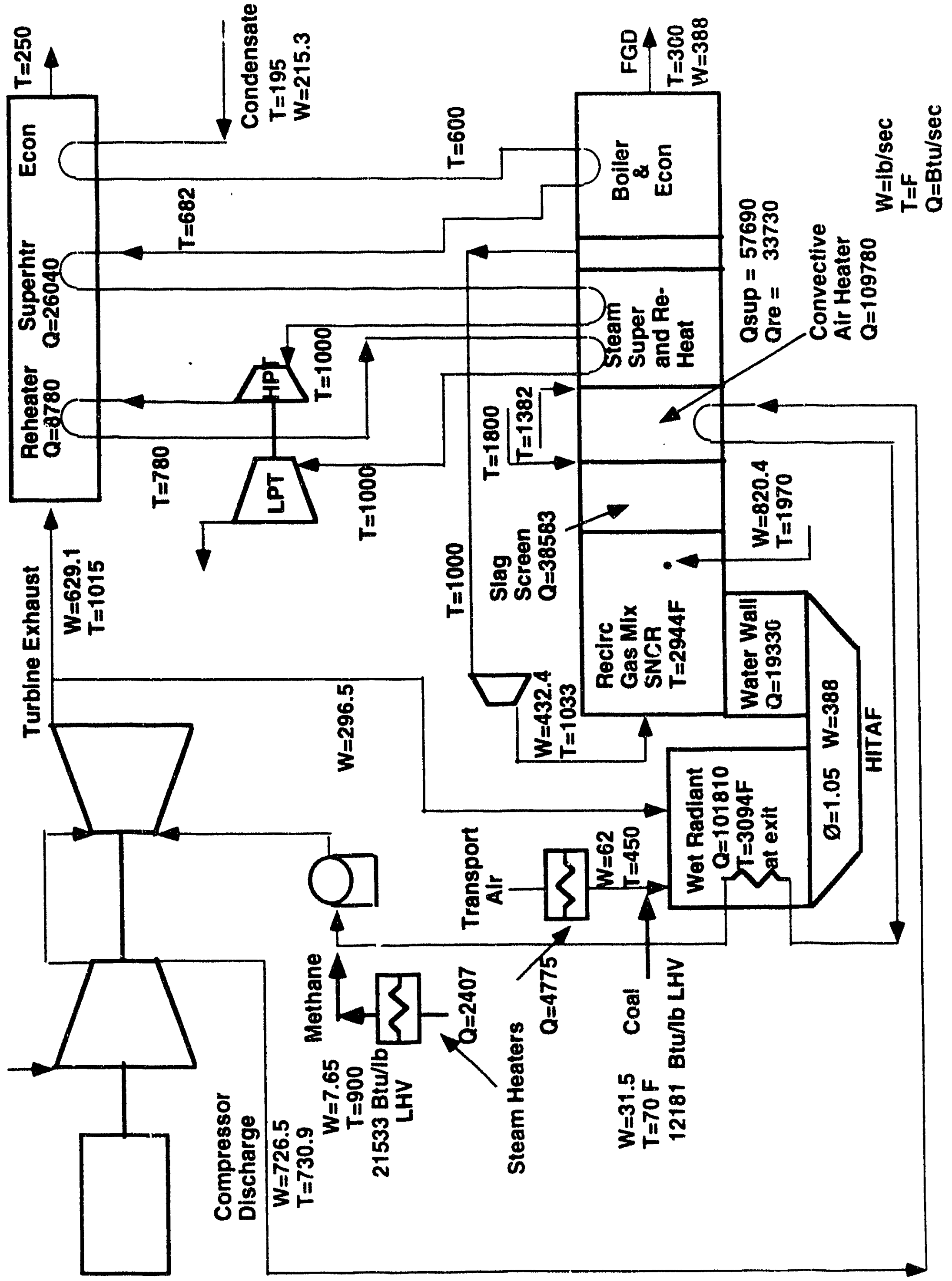

FIGURE 3. SYSTEM FLOWPATH

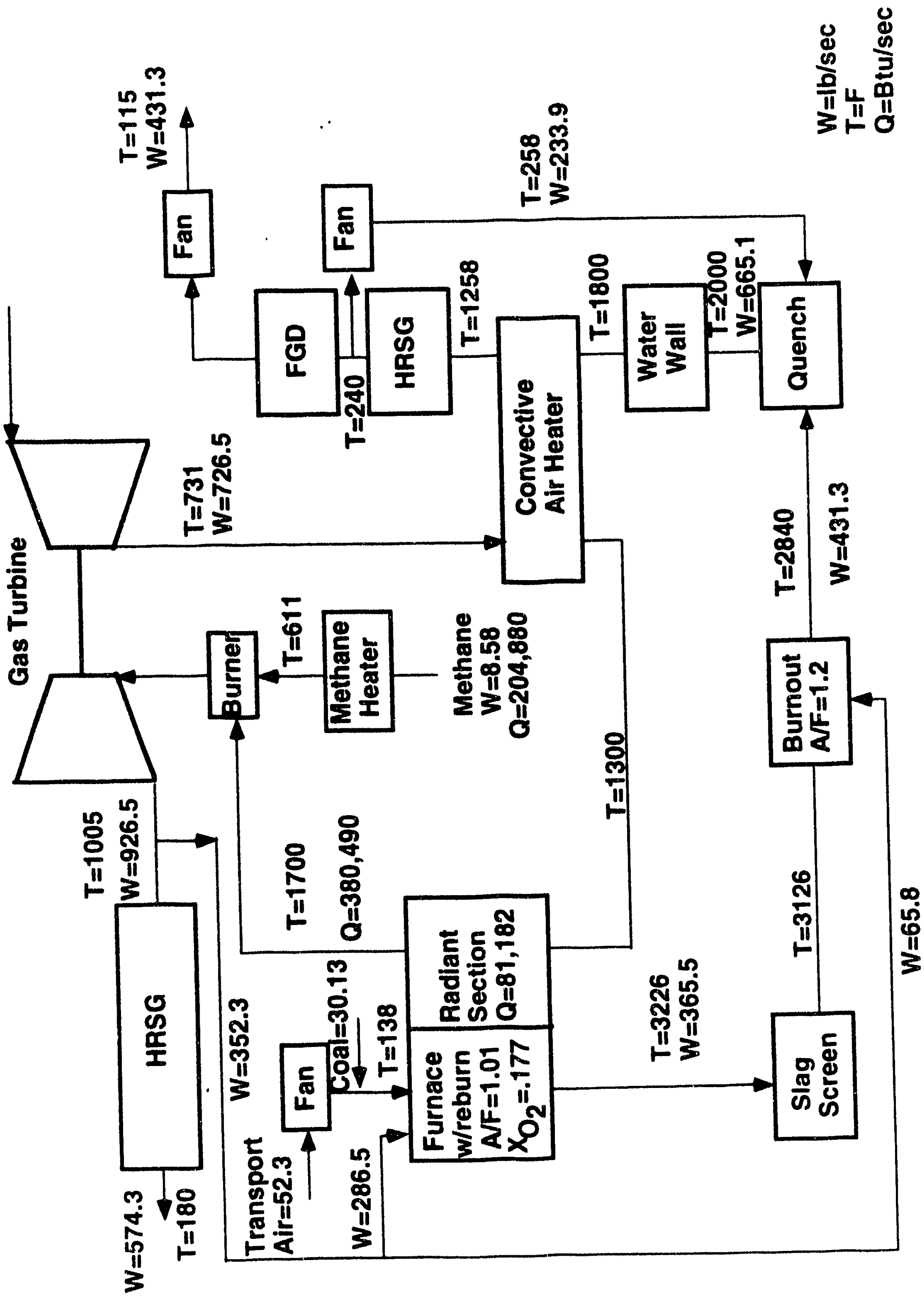

Because of the difference in heating values, the energy needs to be about 11% higher (3340 Btu/sec). Also, the resulting combustion gases are different, requiring an additional 300 Btu/sec, or 3740 Btu/sec of methane flow. To keep the methane/coal split at 35%/65%, the coal flow must be increased by 6946 Btu/sec (HHV). Thus, the total heat input is increased by 10,680 Btu/sec. None of this heat addition results in any significantly greater work in the gas turbine, only in the steam turbine. Stack losses, however, limit the heat available to the steam side to about 6700 Btu/sec which is converted at 35% efficiency. When everything is accounted for, the input to the cycle is up by 1.8% while the output is up by 1.25%, a net decrease of .25 points. Thus, the 35%/65% constraint greatly affects the cycle performance.

It should be noted that the benefit of methane preheater could be realized by either increasing the temperature out of the radiant section by 15 F or by using a Calrod heater either in the methane or in the air stream. The decision concerning the methane heater will be determined by final component layout arrangements.

A number of steam cycles have been investigated including lower pressure (1800 psi) steam cycles with 950F superheat. These systems are less costly than the 2400 psi/1000F/1000F systems and are often a better match to the available waste heat. The resultant performance, however, is lower, definitely not desirable in light of the other cycle changes such as noted above. The current configuration (Fig. 3) has a temperature of 1258F entering the HRSG, certainly high enough to make a 2400 psi/1000F/1000F cycle possible.

Other alternatives considered included different superheat and reheat combinations, e.g., 2400 psi/950F/1050F. While this cycle fit the available heat slightly better than the more conventional 2400 psi/1000F/1000F cycle, its performance advantage was not significantly better and its cost would be slightly higher.

HAT Cycle Analysis

Effort on the HAT Cycle has been delayed somewhat as emphasis has been placed on finalizing the combined-cycle system. Comparison of performances of gas-fired versions of these two cycles with the same level of technology indicate the HAT Cycle to be 1 to 2 points better in efficiency and perhaps at least $100/kW less expensive, depending on NOx levels required. (The combined cycle requires some type of stack gas clean up to meet anticipated future standards for gas-fired plants.)

Using technology slated to be available in aero-derivative engines by the year 2002, HAT Cycle efficiencies have been projected to be near 63% (LHV) for natural gas firing. Some, but not all, of these technologies could appear in heavy frame machines several years later and would result in combined cycle performances of 60-61%, assuming some type of dry low NOx combustor is developed. The HAT Cycle does not need NOx control beyond the humidified air; a CO burnup cell maybe required, however.

TASK 3.1.1 CHEMICAL REACTOR MODELING

Engineering Analysis

A preliminary design, shown in Figure 4, was developed for the HITAF based on the use of cleaned, dry Illinois #6 bituminous coal. The design, based on the long-axial-flame concept is for one 630 MBTU/hr combustor of a required two-combustor system. The facility shown is a down-fired furnace, and the dynamics of the long axial flame assist in minimizing NO_x formation and ash deposition. The deposition of ash on the radiant panels directly impacts the efficiency of the radiant heat exchangers, as previously discussed (see the quarterly progress report for the period 10/1/92 - 12/31/92); therefore, minimizing the deposit formation on the HITAF walls is critical to the overall operation of the combined cycle. Some deposition does occur, however, and the high temperature of air in the radiant heat exchanger panels results in slagging walls; therefore, the combustor is designed with a slag tap at the base of the main combustion zone.The coal feed rate was modified from 70% to 65% of total thermal input, and the remaining 5% is used as natural gas for reburning. The primary and secondary flow rates are set to an overall burner stoichiometry of 0.9, with the burnout air being added to bring the overall stoichiometry back to 1.0. Reburning fuel lowers the stoichiometry to 0.93, and dilution air (flue gas recirculation + turbine exhaust) brings the overall stoichiometry back to 1.2. The injection point for initial burnout air in the radiant section is based on a computed 98% burnout of coal (model predictions). Reburning fuel is added at a distance downstream from the burnout air giving approximately 1 second of residence time for burnout air mixing/combustion.

The length of the main combustion zone is sufficient for complete burnout of coal particles, even with the slow-mixing naturally-staged flame. This length also allows for reburning in the radiant panel zone such that the energy content of the natural gas can be transferred to the heat-exchanger air. Entrained ash is rejected as the combustion gases turn into the horizontal section and pass through a slag screen. The steep slope of the horizontal section is to assist in the transition from wet flowing walls to dry cleanable walls. The combustion gases must be cooled prior to entering the convective heat exchanger and the overall stoichiometry was decreased due to injection of the reburning fuel. To cool the combustion gases and increase the overall stoichiometry, a mixture of flue gas at 300F and turbine exhaust at 1000F is added towards the end of the horizontal section, bringing up the overall oxygen concentration and lowering the temperature of the combustion gases. Additional heat removal is accomplished via waterwalls installed in the base of the convective section.The combustion gas temperature at the exit of the waterwall section is appropriate for selective non-catalytic reduction (SNCR) reactions for NO_x control; therefore, urea injectors are installed at this exit and an adiabatic section allowing substantial residence time for reduction reactions exists prior to the convective heat exchanger. It would be desirable to minimize the distance between the injectors and the convective heat exchanger, and to allow for SNCR reactions within the convective heat exchanger passages; however, the temperature of combustion gases drops rapidly within the short residence time of the heat exchanger resulting in rapidly decaying NO reduction rates.The offset of the convective heat exchanger and SNCR duct from the main combustor, shown at the top of Figure 4, allows access to all sides of the HITAF for maintenance and minimizes the transitional distance between the main combustion chamber and the convective section. In addition, this configuration facilitates connections to and the placement of the gas turbine between two opposing HITAF structures.

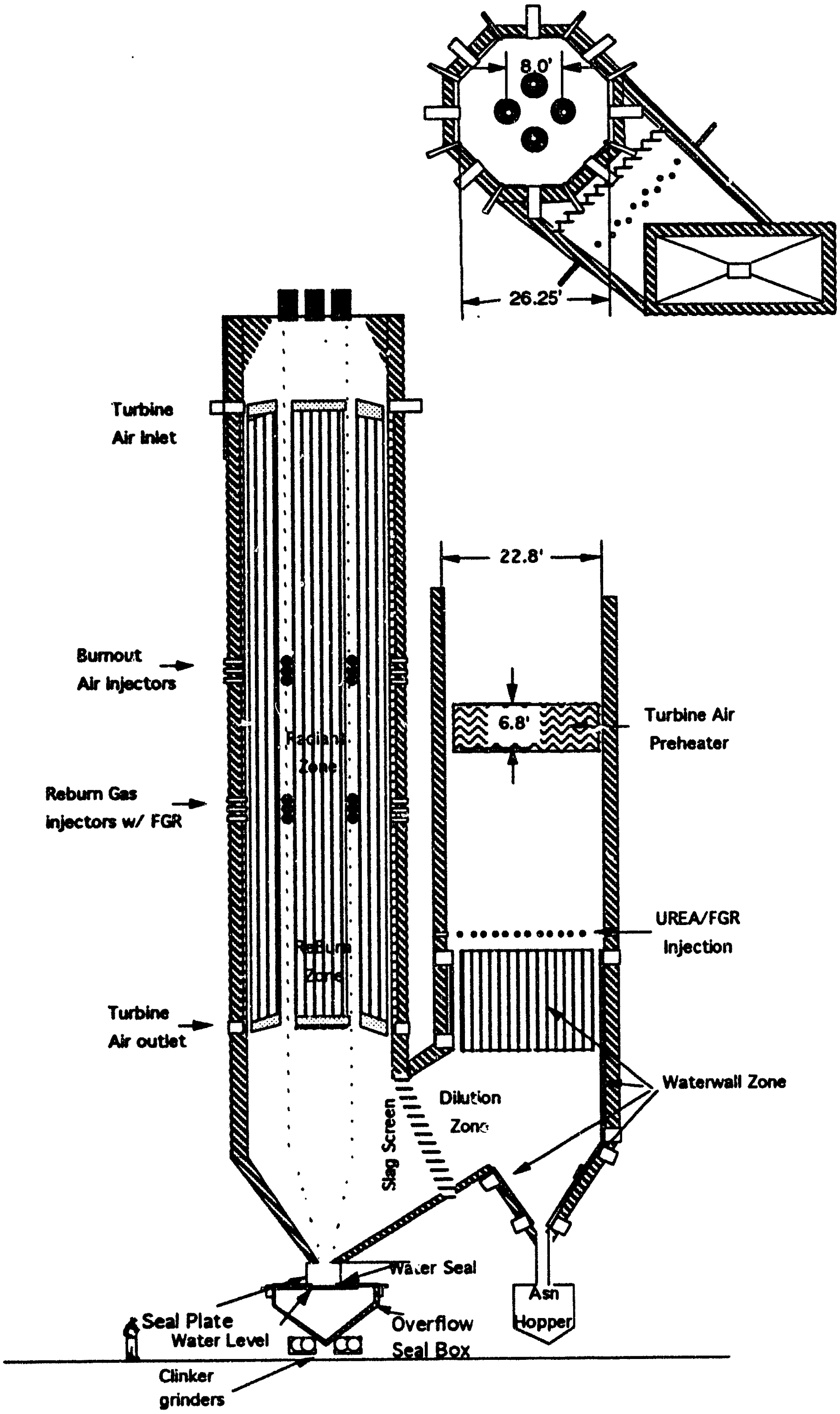

Figure 4. Drawing of the long axial flame HITAF design.

Experimental System

The experimental effort to provide data for validating the combustor modeling and evaluating the NO_x control concepts, is being carried out in the 100,000 BTU/hr combustion research facility at the University of Utah. A cross-sectional view of the "U"-shaped facility (Figure 5) shows clearly the details of the furnace. The test facility is equipped with a multitude of access ports over the entire length of the combustion chamber (detailed in Figure 5) which allow extensive testing of various staging and reburning configurations. In addition, the large single section on the right, or outlet side of the "U" facility is fitted with auxiliary burners in isolated combustion chambers allowing for the maintenance of an isothermal reaction zone for SNCR testing. The facility has the option of using preheated combustion air or high temperature vitiated air from a gas-fired hot-gas generator.

Preliminary Experimental Results

The initial experimental studies focus on characterizing the impact of combustion parameters on NO_x emissions under conditions specific to the HITAF concept. In particular, these studies are investigating the effects of:

- Vitiated air with 1000 °F preheat.
- Axial fuel injection with gas stabilization.
- Coal particle size distribution and coal type.
- Hybrid in-furnace NO(x) control schemes

In each case, emphasis is placed on optimizing the individual zone performance to minimize the overall NO_x emissions from the combined system. All of the experiments reported in this section were conducted with a Utah bituminous coal, firing at 90,000 BTU/hr. The secondary air was preheated to 650F and was introduced axially; no swirl was used in these experiments. The primary air was held constant at approximately 15% of the stoichiometric requirement and was not preheated. The overall excess oxygen in the exhaust was held at 3%.

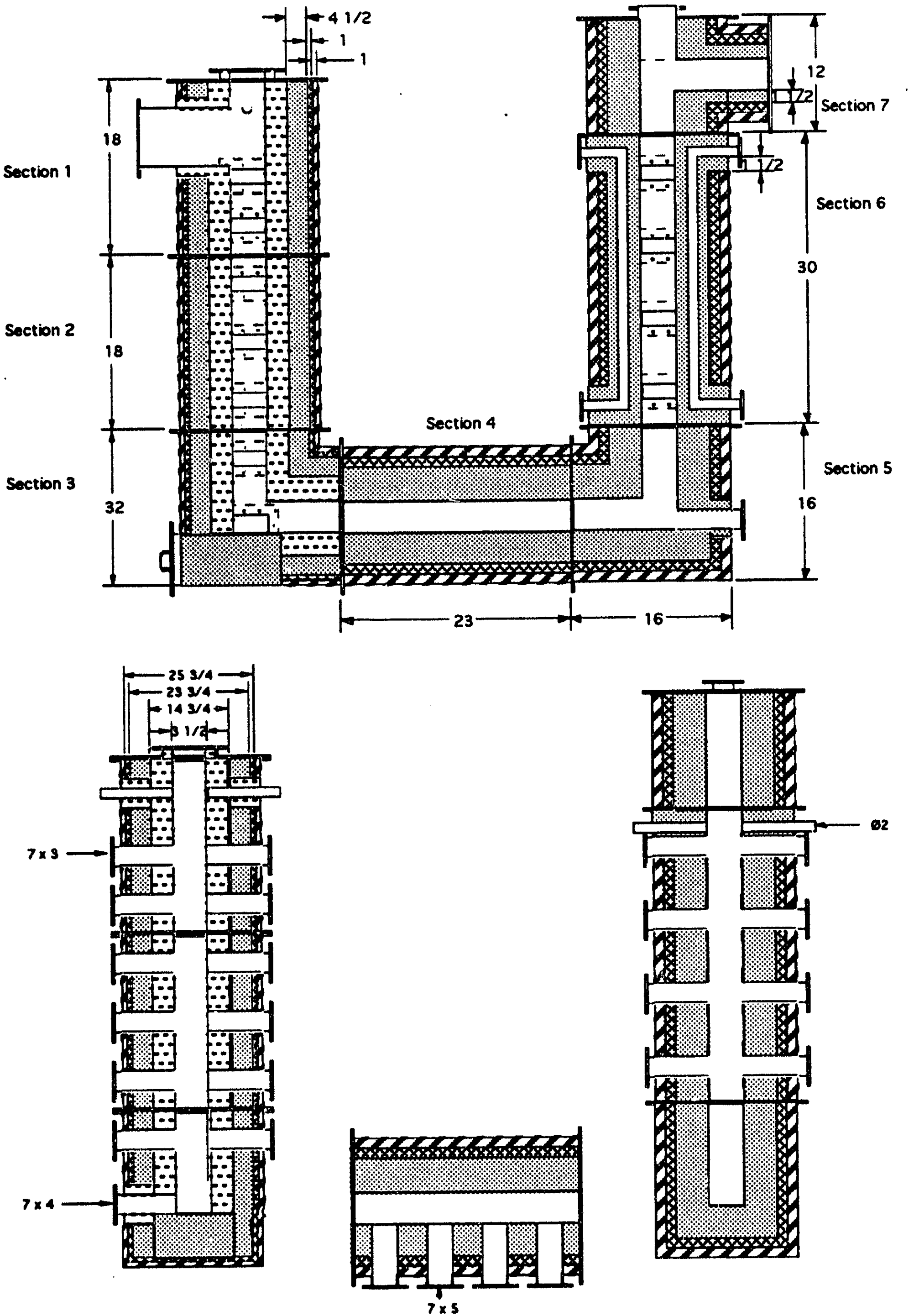

Figure 5. Schematic of the 100,000 BTU/hr experimental test facility at the University of Utah. The down-fired burner is on the left of the "U"-shaped design, and the isothermal test section is on the right side side of the "U". The end views show the placement of access ports throughout the facility. All dimensions are in inches.

Research funded by the EPA at the International Flame Research Foundation in the early seventies [1] identified the importance of near-burner fuel/air mixing, and the point of flame stabilization on NO formation in pulverized coal flames. Axial fuel injection tends to naturally retard near-field mixing and thereby reduce NO_x emissions, relative to fuel injection schemes which direct the fuel radially outward into the secondary air. However, if the point of ignition of the axial fuel jet is displaced, significant secondary-air entrainment can occur prior to ignition, thus increasing the oxidation of fuel nitrogen within the core of the fuel jet. If the ignition occurs at the injector tip, the entrainment is greatly decreased and NO_x emissions decrease.

In this study, varying amounts of natural gas were injected through five axial holes around the outside of the primary air/coal stream, to provide positive anchoring of the axial flame. As the data in Figure 6 indicate, flame anchoring can have a major impact on NO_x emissions. With all axial secondary air and axial coal injection (0% natural gas), the coal flame is lifted approximately 30 cm from the fuel injector tip and the NO_x emissions are relatively high (850 ppm). Addition of small amounts of gas do not immediately pull the flame back onto the injector tip: however, once sufficient gas is added, the flame front moves back and the emissions drop dramatically. Further, once the flame has been located, only a small amount of gas is required to maintain ignition at this point. As the data indicate, 5% gas is quite sufficient to maintain this ignition and this value was used in all subsequent studies.
Similar test were also conducted on the effects of primary and secondary air flow rate variations and, as expected, increasing the primary air increased NO_x emissions significantly. Increasing secondary air (and hence overall excess air) also increased NO_x emissions but less dramatically.

Figure 7 shows the effects of staging and reburning on NO_x emissions with the gas-stabilized axial flames. Decreasing the primary zone stoichiometry from 1.15 (no staging air) to approximately 0.95 reduced the emissions from 400 ppm to just below 200 ppm. Similar reductions have been reported previously by other investigators for conventional flames [2, 3] but the optimum stoichiometry was found at more fuel-rich conditions (0.6-0.7). This apparent shift in optimum stoichiometry is likely due to the fact that the gas-stabilized axial flames are naturally-staged due to the slow fuel/air mixing.
Figure 7 also shows the application of natural gas reburning to this system. For natural gas additions to the levels shown (reburning zone stoichiometry), it was possible to reach emission levels below 150 ppm NO_x without the use of selective NO_x reduction agents. In this case, natural gas was used as the reburning fuel and was injected at the same point as the second stage air in the previous experiments (at port #1 in furnace section 3 in Figure 2), about 2 meters downstream from the point of coal injection. In the reburning tests, the final burnout air (to a level of ~3% O_2 in the flue) was added at port #1 in section 4 (about 1 meter downstream from the point of reburning gas injection). At the minimum NO_x conditions, approximately 10% of the total fuel input was reburning gas.

The initial experimental results demonstrate the potential of the gas-stabilized axial flame to produce low NO_x emissions under staged combustion conditions. Future work will focus on optimizing the application of reburning and selective reduction agent addition to minimize the emissions from the overall process, and in order to reach NO_x emissions levels below 100 ppm .

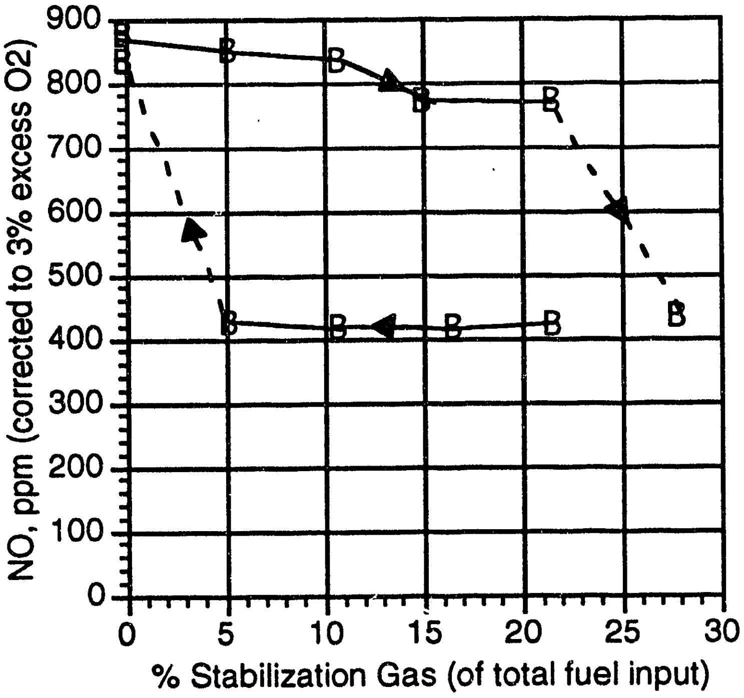

15% Primary Air

Figure 6 Effect of axial natural gas addition on NO emissions in a naturally-staged flame.

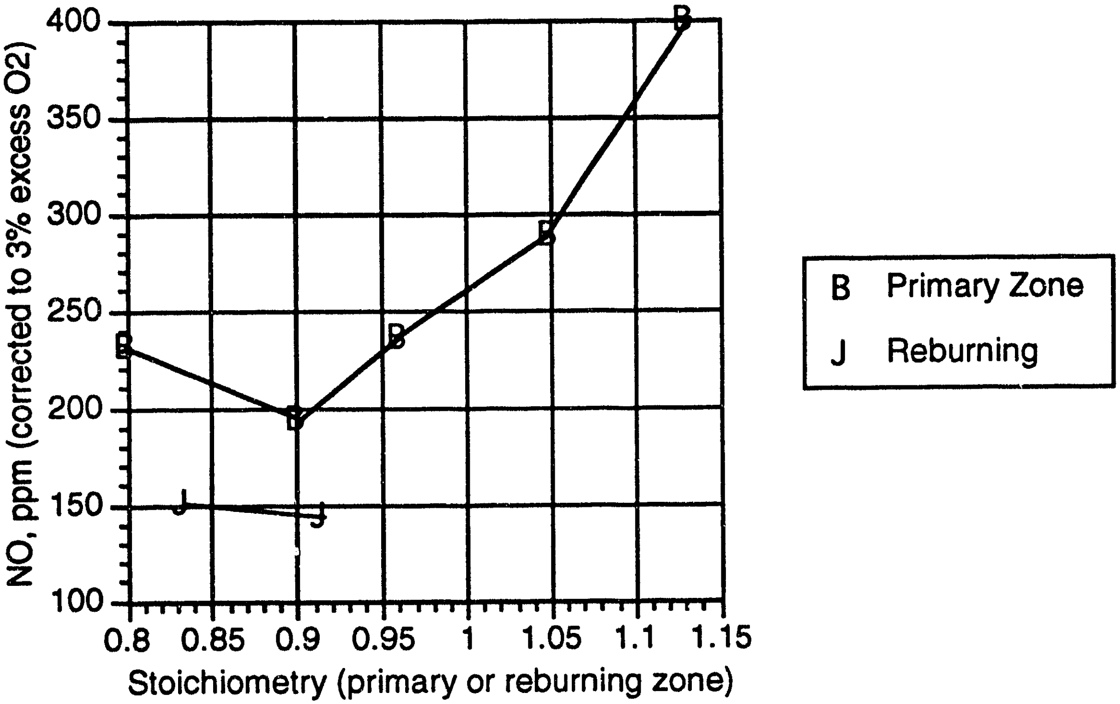

Figure 7. Impact of stoichiometry changes in the primary zone for a staged axial flame. Also shown are the results obtained for downstream reburning at two different stoichiometries.

TASK 3.1.2 AIR HEATER DESIGN

The air heater designs are being refined so as to include more realistic models for slag flow and thermal resistance on the radiant air heater and ash deposition on the convective air heater.

Radiant Air Heater Model

The radiant air heater model has been modified to include a comprehensive treatment of ash deposition and formatin of a falling slag layer film. Whereas the radiant heater model which was described in a previous report included a specified slag layer of constant thickness and a dry ash layer which depended on the temperature of the layer, the newest model accounts for the buildup of both the liquid slag and dry ash layers over the heater length with variable viscosity in the slag layer and freezing behavior of the slag to form a dry ash layer. In addition, the modified model simulates heat release due to combustion over the length of the radiant furnace rather than allowing the flue gas temperature to decrease by a simple heat balance relative to the radiant heat transfer. The main features of this revised slag layer model are described below and some important predictions from the new model follow.

The development of the equations which govern the gravity-induced flow of a slag layer on a vertical surface as shown in Fig. 8 have been extracted from the PhD thesis of Rodgers [4]. Since inertial forces and the pressure gradient are neglibible for a falling film at low Reynolds number with a free surface, the equation of motion (x-direction) for the slag layer is simple

$$\frac{\partial \tau}{\partial y} = \rho g \tag{1}$$

where τ and ρ are the viscous shear stress and mass density of the slag layer, respectively, and g is the gravitational constant. By further assuming that the slag can be represented as a Newtonian fluid, the viscous sheat stress for the slag is related to the viscosity, μ by the expression

$$\tau = \mu \frac{\partial u}{\partial y} \tag{2}$$

where u = u (x,y) is the velocity of the slag layer in the y-direction, the equation of motion can be rewritten as

$$\frac{\partial}{\partial y} \left(\mu \frac{\partial u}{\partial y}\right) = \rho q \tag{3}$$

FIGURE 8. GRAVITY-INDUCED FLOW OF A VISCOUS SLAG LAYER DOWN A SOLID SURFACE

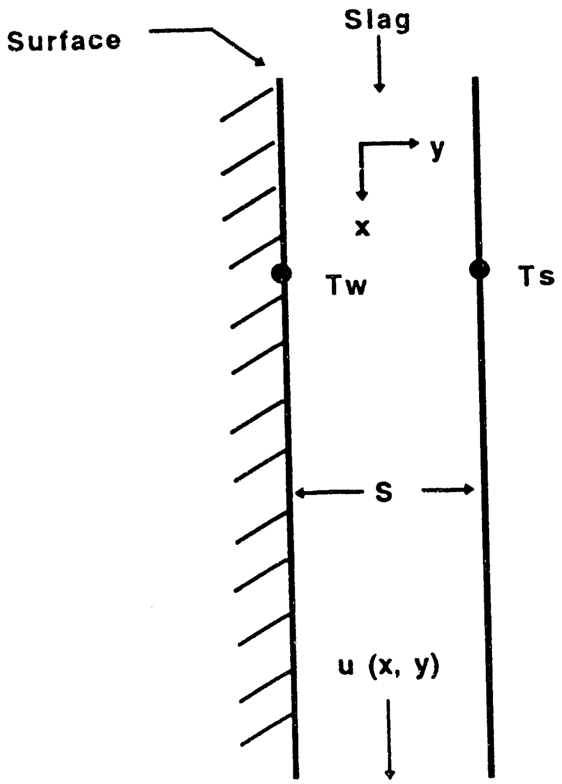

Since energy exchange due to convectin and viscous dissipation are negligible for lay Reynolds number flow and heat conduction across the slag layer is the dominant energy transport mechanism, the energy conservation equation for the slag layer is simply

$$q = k \frac{\partial T}{\partial y} \tag{4}$$

where q = q (x,y) is the heat flux normal to the slag layer, k is the thermal conductivity of the slag, and T = T(x,y) is the temperature of the slag.

The boundary conditions chosen for the above set of governing equations are as follows:

$$u(x,0) = 0$$

$$T(x,0) = T_W(x)$$

$$\tau(x,s) = q_S(x,s) = \text{free surface shear force (assumed to be 0)}$$

$$q(x,s) = q_S(x,s) = \text{free surface heat flux from the gas phase}$$

where s is the thickness of the slag layer. The free surface shear force is assumed to be zero because the flue gas velocity in the radiant furnace is expected to be very low. If the flue gas velocity is significant, a correlatin for the free surface shear stress can easily be included in the model.

Finally, the sum of the deposition of ash from the gas phase, which is given by the expression

$$\dot{M}_s(x) = \int_0^x \dot{m}_s(z)\, dz \tag{5}$$

must be equal to the mass flux of slag at any axial position y, which is given by the expression

$$\dot{M}_s(x) = \int_0^s \rho\, u(x,y)\, dy \tag{6}$$

as long as the slag layer has not begun to freeze. However, if the viscosity of a portion of the slag layer is lessw than the critical viscosity, as indicated by the temperature of the layer, that portion of the layer is assumed to have frozen and the mass flux of slag given by Eq. (5) is corrected for the solid slag.

A numerical solution has been developed for the above set of equations which describe the development, flow, and heat transfer across a falling slag layer film. This numerical solution is based on transforming the governing equations with respect to the independent variables of the (x,y) coordinate system

$$\frac{\partial y}{\partial T} = \frac{k}{q(x, T)} \tag{7}$$

$$\frac{\partial u}{\partial T} = \frac{k\,\tau}{\mu\, q(x, T)} \tag{8}$$

Examination of Eq. (7) and the relevant boundary conditions leads to the following results

$$\frac{\partial q}{\partial T} = 0 \tag{9}$$

and $q(x,T) = q_s\,(x,T_s)$ = the net radiant heat flux from the gas phase.

Also, from Eq. (7), the slag layer thickness, s, is given by the expression

$$s(x) = \frac{k\,(T_s - T_w)}{q_s(x, T_s)} \tag{10}$$

To complete the slag layer model the density, r, and thermal conductivity, k, of the slag are assumed to be constant while the viscosity of the liquid slag is assumed to vary with temperature according to the following expression

$$\mu = A\ T^n\ e^{B/T} \tag{11}$$

where A, B, and n are coefficients for the particular ash.

By transforming the equation of motion, Eq. (3), using Eq. (7), and integrating with respect to temperature, the viscous shear stress in the slag layer is given by

$$\tau(x, T) = \frac{\rho\, q\, k\,(T_s - T)}{q_s(x, T_s)} + \tau_s \tag{12}$$

where $\tau_s = 0$.

Then by substituting Eq. (12) into Eq. (8) and integrating again with respect to temperature, the velocity profile for the liquid slag layer is given by

$$u(x,T) = \rho q\left[\frac{k}{q_s(x,T_s)}\right]^2 \int_{T_w}^{T} \frac{(T_s - \theta)}{A\ \theta^n\ e^{B/\theta}}\ d\theta \tag{13}$$

Finally, by substituting Eq. (13) into Eq. (6), the mass flux of liquid slag at any axial position is

$$\dot{M}_s(x) = \frac{\rho k}{q_s(x,T_s)} \int_{T_w}^{T_s} u(x,\theta)\ d\theta \tag{14}$$

The numerical procedure developed to simultaneously solve for the net radiant heat transfer, from the flue gas stream to the air stream, and the liquid slag layer thickness, and its related characteristics, at each axial position of the radiant air heater is as follows:

(1) Assume the thickness of the liquid slag layer. At the top of the radiant air heater, at $y = 0$, the slag layer thickness is defined to be zero. For $y>0$, the slag layer thickness at the previous axial position is a good initial assumption for subsequent axial positions.

(2) Using an iterative procedure based on the radiation and conduction equations for the radiant air heater model, which was described in a previous report, compute the surface temperature of the slag layer and the net heat flux from the flue gas to the air.

(3) Compute the velocity profile in the slag layer using Eq. (13).

(4) Compute the mass flux of liquid slag using Eq. (14).

(5) Compute the sum of the deposition of ash from the gas phase which is in the liquid layer; from the total amount of ash which has deposited on the radiant air heater, given by Eq. (5), subtract the amount of slag which has frozen, as defined by the portion which is at a viscosity greater than the critical value. Actually, the temperature corresponding to the critical viscosity, Tcv, is used for this determination of the frozen slag fraction.

(6) Compare the mass flux of liquid slag, computed in (4), with the sum of the deposition of ash from the gas phase which is in the slag layer, computed in (5). If these computed values for the slag mass flux agree within a reasonable tolerance (0.1% should be acceptable), the assumed slag layer thickness is correct.

(7) Repeat the above procedure until accurate and consistent values have been computed for the slag layer thickness, surface temperature, and other pertinent characteristics of the radiant air heater.

Using data from Reid and Cohen [5], the following equation was derived for the viscosity of ash produced from Illinois 6 coal under oxidizing conditions where the viscosity, μ, is in poise and the temperature is in Kelvin. This equation should be valid for the temperature range from 1475 to 1700K (2195 to 2600F). Based on a correlation by Hoy, et. al, [6], the critical viscosity for ash produced from Illinois 6 coal under oxidizing conditions occurs at a temperature of 1498K (2237F).

Radiant Air Heater Performance

The improved radiant air heater model, which accounts for ash deposition, a falling liquid slag layer and slag freezing when the slag viscosity drops below a critical value, was used to gain further insight into the proper operation of a radiant air heater. These modeling studies were performed for the following set of fixed or constant parameters.

Air temperatures (F)	1300 (in)/1800 (out)
Furnace diameter (ft):	26.5
Radiant gas diameter (ft):	20
Mass flow rates (lbm/hr):	1,307,000 (air) 561,500 (gas)
Ash temperature at critical viscosity (F):	2237
Air heat transfer coefficient (Btu/hr-ft2-R):	100
Thermal conductivities (Btu/hr-ft-R):	30 (SiC wall) 6.4 (refractory) 2.0 (dry ash) 2.0 (slag)
SiC wall thickness (inches):	0.25
Refractory thickness (inches):	1.0
Emissivity of gas:	0.90
Emissivity of slag:	0.65
Ash deposition flux (lbm/ft2-hr):	0.005234 (base case)

Two extreme cases for the flue gas temperature were used in these radiant air heater modeling studies: (1) variable flue gas temperature; based on radiant heat transfer and a simple energy balance without heat generation, and (2) constant flue gas temperature; assuming heat release due tyo combustion equals radiant heat transfer. For both of these cases, the radiant air heater would be preceeded by an adiabatic section which would allow the flue gas temperature to increase to the required level due to combustion before radiant heat transfer occurs. In addition, two flow arrangements were considered: (1) parallel flow; where both the air and the flue gas enter at top of the furnace, and (2) counter flow; where the flue gas enters at the top of the furnace and the air enters at the bottom of the furnace.

The effects of a constant flue gas temperature on the radiant air heater length and slag and dry ash layer thicknesses are shown in Figs. 9 and 10 for the two flow arrangements. As expected, the radiant air heater length and slag and ash layer thicknesses all increase with decreasing flue gas temperature. Although the maximum slag layer thickness increases slowly with decreasing gas temperature for both flow arrangements, the dry ash layer thickness increases abruptly for gas temperatures below about 2700 F. While the differences between the flow arrangements are small for higher flue gas temperatures of the order of 3000F, the differences are significant for lower gas temperatures of the order of 2600F. Moreover, the particularly large differences in slag and ash layer thicknesses for the two flow arrangements at the lowest temperature suggests that the parallel flow arrangement is favored because the slag layer flows more readily and the dry ash layer is less likely to form. However, the counter flow arrangement results in a slightly shorter radiant air heater at the lowest gas temperature because the thermal resistance is very low at the top of the heater. In either case, however, the flue gas temperature must be maintained above about 2800F to avoid freezing of the slag and formation of thick layers of dry ash.

Figures 11 to 13 show the temperature profiles throughout the structure of the radiant air heater as a function axial position for both flow arrangements with a constant flue gas temperature of 2800F and for parallel flow with a variable flue gas temperature which starts at 3400F. The slag and ash layer thickensses corresponding to these three cases are shown in Fig. 14. For a constant gas temperature of 2800F, the temperature profiles for the two flow arrangements are essentially the same but reversed with axial position. Although the slag layer thickness gradually increases for both flow arrangements, the slag for the counter flow arrangement is about twice as thick as for parallel flow. As noted above, dry ash doesn't form for either flow arrangement at this gas temperature. In contrast, for the case of variable flue gas temperature and parallel flow (Fig. 13), the heater length is much larager than for the constant gas temperature cases because a very thick layer of dry ash forms. This last result suggests that heat additin by combustion over the length of the radiant air heater is required to avoid the undesirable effects due to freezing of the slag, formation of dry ash, and the resultant high thermal resistance.

For the cases with constant flue gas temperature of 2800F (Figs. 11 and 12), note that the maximum temperatures of the SiC wall and the refractory are 2100F and 2500F, respectively, which should be reasonable temperature requirements for these materials. Alternatively, the wall temperature could be lower and the refractory temperature higher if the refractory is thicker. However, if the wall temperature is lowered, the radiant air heater would have to be longer and/or the air side heat tranfer coefficient would have to be higher, both of which will require additional pressure drop. Inasmuch as material temperature requirements, air heater size, air side pressure drop, and flue gas temperature are all interdependent, a parametric study of these and other characteristics of the radiant air heater will be conducted for the next report.

The effects of higher levels of ash deposition flux on the performance characteristics of the radiant air heater are shown in Fig. 15 for the case of parallel flow with a constant flue gas temperature of 2800F. For this case, as the ash deposition flux is increased by a factor of one to ten, the radiant air heater length increases by only five percent while the liquid slag layer thickness doubles and still no dry ash layer is formed. These results can be explained by noting that the flue gas temepratute is sufficiently high that the slag layer temperature never drops to the value at the critical viscosity, ensuring that the slag flows readily and no dry ash forms.

In summary, these model results clearly show that the formation of thick layers of dry ash on the radiant air heater can be avoided by maintaining a nearly constant flue gas temperature of about 2800F or higher over the length of the heater. Although this will require an adiabatic combustion section before the radiant air heater and continuous heat release by combustion over the length of the heater, this concept is consistent with the radiant furnace design which utilizes a long, naturally-staged combustion process.

FIGURE 9. RADIANT AIR HEATER LENGTH VS. CONSTANT FLUE GAS TEMPERATURE

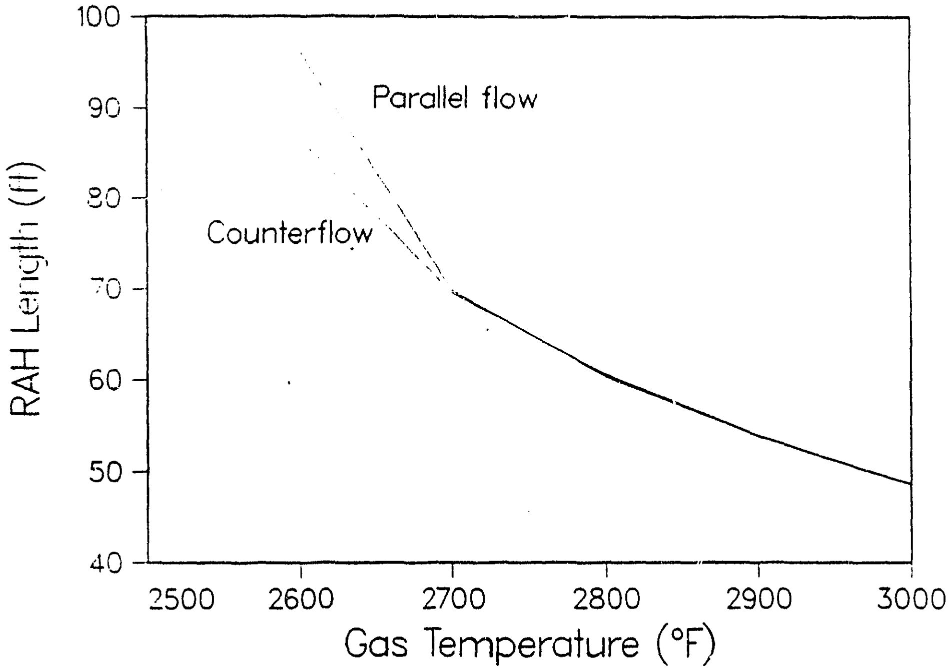

FIGURE 10. MAXIMUM SLAG AND ASH LAYER THICKNESSES VS. CONSTANT FLUE GAS TEMPERATURE

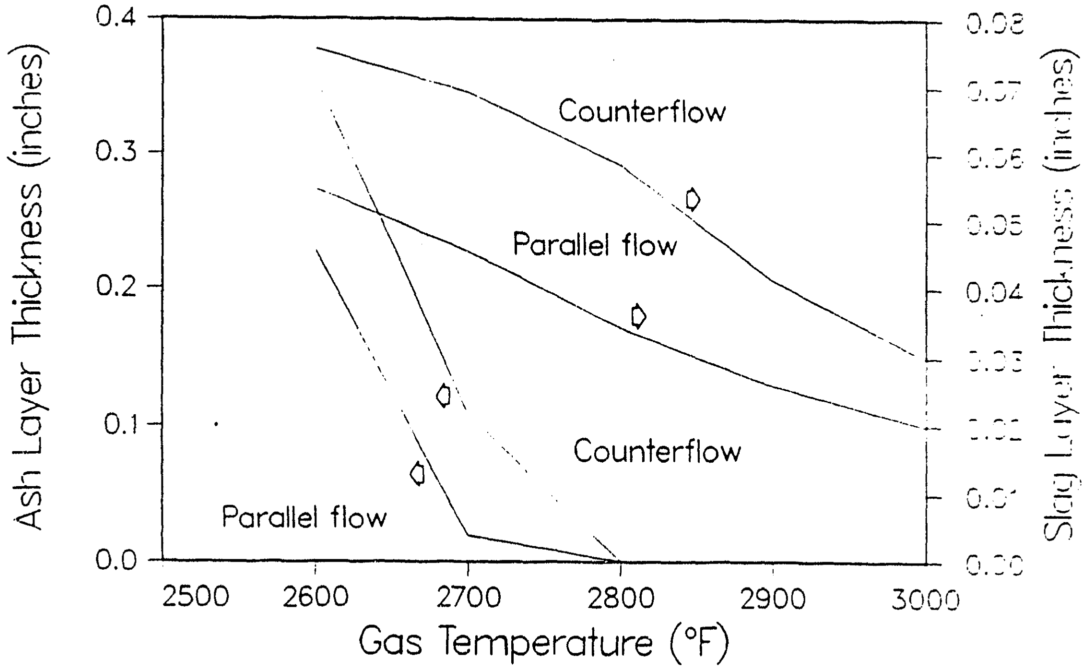

FIGURE 11. RADIANT AIR HEATER TEMPERATURE PROFILES--CONSTANT FLUE GAS TEMPERATURE (2800°F); PARALLEL FLOW ARRANGEMENT

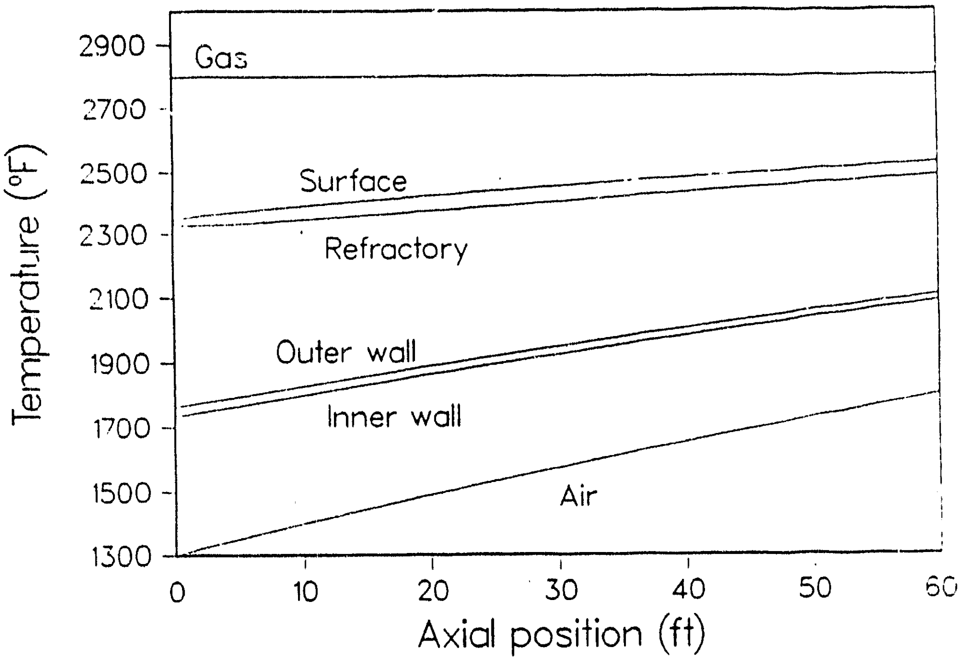

FIGURE 12. RADIANT AIR HEATER TEMPERATURE PROFILES--CONSTANT FLUE GAS TEMPERATURE (2800°F); COUNTERFLOW ARRANGEMENT

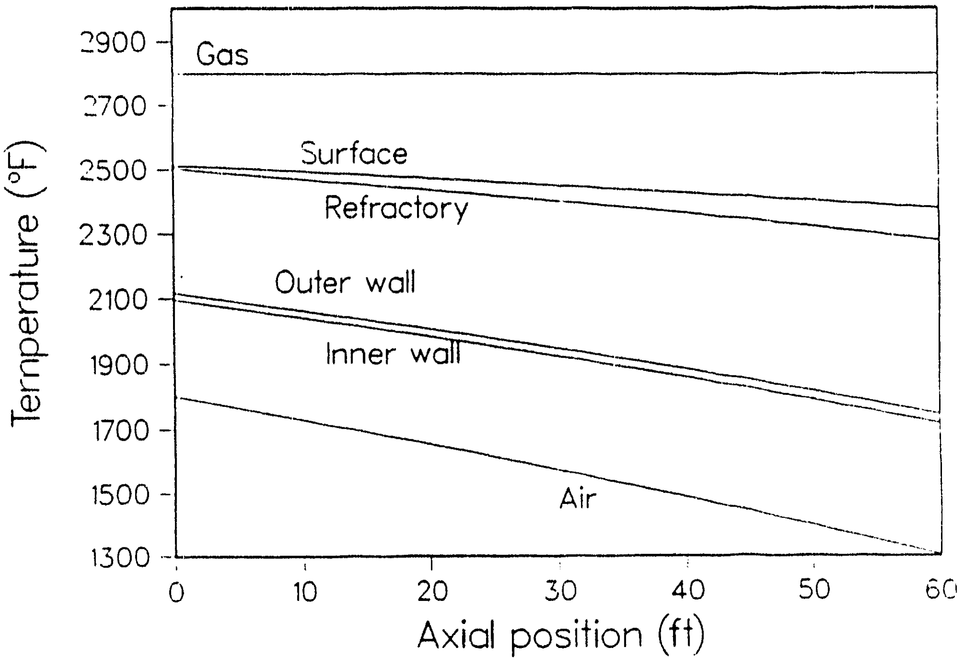

FIGURE 13. RADIANT AIR HEATER TEMPERATURE PROFILES--VARIABLE FLUE GAS TEMPERATURE (3400°F) PARALLEL FLOW ARRANGEMENT

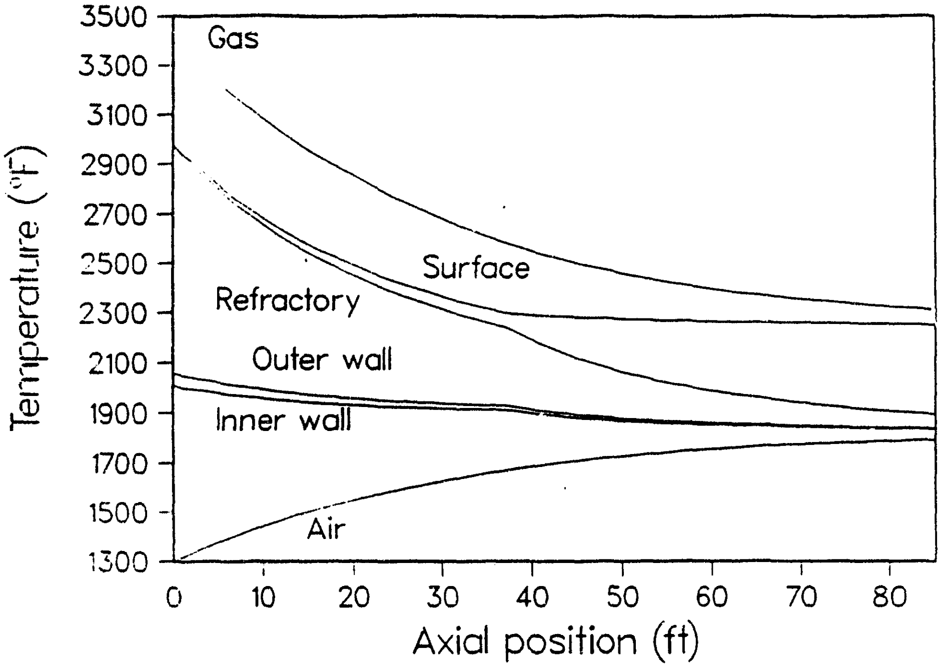

FIGURE 14. RADIANT AIR HEATER ASH AND SLAG THICKNESS

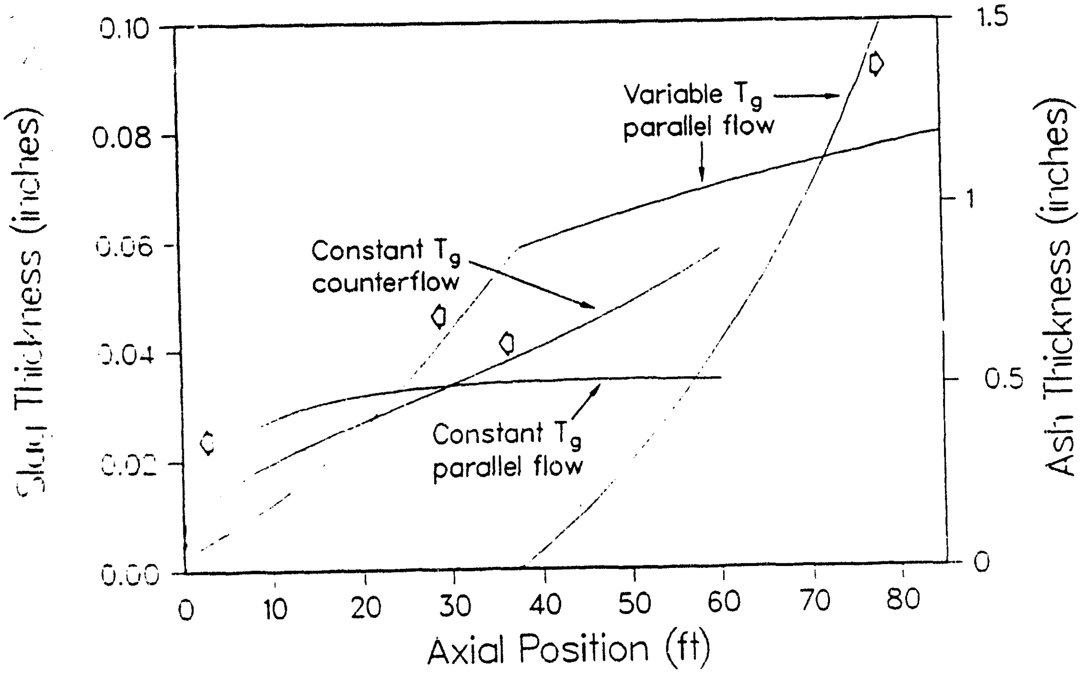

FIGURE 15. EFFECT OF ASH DEPOSIT FLUX ON RADIANT AIR HEATER SIZE PARALLEL FLOW ARRANGEMENT/2800°F FLUE GAS

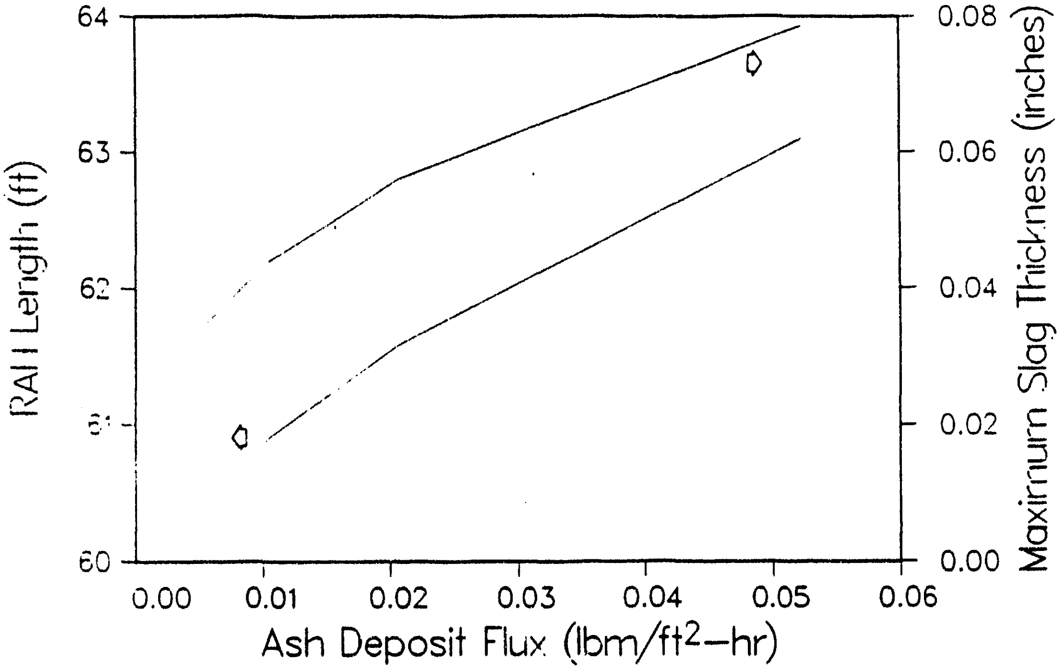

TASK 3.2.2 MINERAL/ASH TRANSFORMATIONS

Experimental

Five series of experiments were carried out using two different types of silicon carbide and two different types of coal ash. NT-230 is a siliconized silicon carbide manufactured by Norton. Hexoloy SA is a sintered alpha-silicon carbide manufactured by Carborundum. The experimental apparatus for the alkali corrosion experiments was described in Quarterly #3. The siliconized silicon carbide (Norton NT-230) was tested at 1173 and 1248 K. The sintered silicon carbide (Carborundum Hexoloy SA) was tested at 1248 K. Results of the experiments at 1173 K were reported in Quarterly #3. Illinois 6 ash is high in silica and iron, while Wyodak ash is lower in silica and high in calcium and magnesium. Experiments were performed using the size segregated ash. After the exposure test, each sample was set in epoxy resin and cut in half. The cross-sections were examined via SEM and EDX analysis at EERC. Elemental composition was determined at individual points or mapped over the entire image.

Sodium Sulfate-Ceramic Interactions

Sample B.1 consisted of a layer of sodium sulfate on NT-230 silicon carbide subsequently exposed to vapor-phase sodium sulfate at 1248 K. The sample shows a reaction layer containing bubbles, some several hundred microns large, sitting on top of the silicon carbide substrate. As seen in Figure 16, this reaction layer is on the order of 50 microns thick. Element maps reveal that the reaction product is a mixture of sodium silicate and pure silica. A few areas of sodium sulfate can be seen, but very little sodium sulfate remains on the surface.

The next set of samples to be analyzed consisted of Hexoloy SA substrates tested at 1248 K. Sample C.1 consisted of an initial layer of sodium sulfate (5 mg/cm^2) on Hexoloy. A thick reaction layer (100 to 200 mm) was observed on top of the silicon carbide. This layer contains large bubbles and distinct composition regions of pure silica and sodium silicate, similar to the NT-230 sample B.1. Element maps show a silica layer at the silicon carbide interface and on top of the sodium silicate layer. A small amount of sodium sulfate can be seen on top of the reaction layer. Qualitatively, sample C.1 appears the same as sample B.1, indicating that the mechanism for reaction with sodium sulfate is the same in both materials. Quantitatively, the Hexoloy sample C.1 shows a thicker reaction layer than the NT-230 sample B.1 which seems to indicate that the Hexoloy reacted more extensively with sodium sulfate than did the NT-230.

FIGURE 16. SEM PHOTOGRAPH OF NT-230 AFTER REACTION WITH SODIUM SULFATE AT 1248K

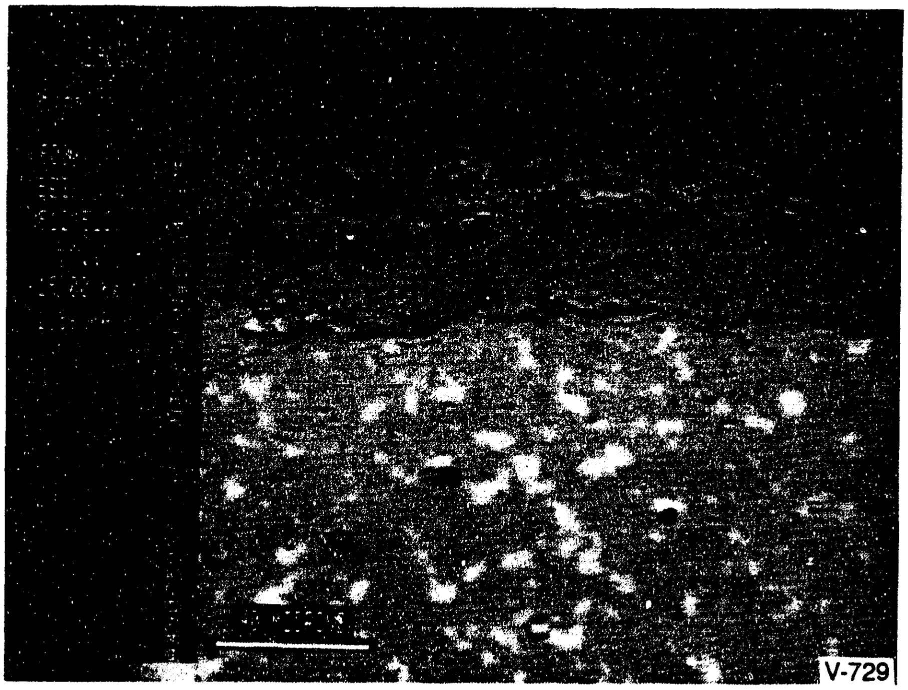

Ash-Ceramic Interactions

Sample B.2 consisted of Wyodak ash only on a siliconized SiC substrate (NT-230) after treatment at 1248 K (Figure 17). The Wyodak ash appeared to partially fuse into larger (50 to 200 mm) masses, similar to the result at 1173 K. The ash shows light areas which appear to be high in sulfur ($CaSO_4$ or sulfated calcium aluminate) and, in some cases, phosphorous. Al, Mg, and Fe are evenly distributed throughout the ash layer. There is a thin (approximately 2 microns) layer of calcium silicate on the silicon carbide surface, indicating that calcium in the ash has reacted with the silicon carbide. Analysis of sample C.2 which contained Wyodak ash on a Hexoloy substrate did not show any reaction product or any remaining ash. Thus, unlike the NT-230 sample, Wyodak ash did not react with Hexoloy SA at 1248 K.

Two sets of experiments were performed at 1248 K using Illinois 6 ash (< 6mm) with NT-230 and Hexoloy substrates. As with the Wyodak ash, the Illinois 6 ash on the NT-230 substrate (sample D.2) fused into large pieces on the order of 100 microns in diameter. In contrast to the Wyodak ash (sample B.2), no oxide layer is visible on the silicon carbide surface. The Wyodak sample had a calcium silicate reaction layer on the surface with a thin silica layer beneath it. No such layers are visible in the element maps for sample D.2 Thus the calcium in the Wyodak ash appears very reactive with the silicon carbide surface. Since Illinois 6 does not contain much calcium, no reaction is observed in sample D.2.

The Illinois 6 ash in sample E.2 appears the same as that in sample D.2: the initial fine ash particles have fused into 100 mm structures. There is no surface oxide layer visible in the element maps. Thus, Illinois 6 ash did not react with either Hexoloy SA or NT-230 at 1248 K over a 200-hr time period.

Ash-Ceramic Interactions with Excess Sodium

Sample B.3 consisted of a layer of sodium sulfate deposited on NT-230 with Wyodak ash on top of the sodium sulfate. Analysis reveals extensive reaction between the Wyodak ash and sodium sulfate at 1248 K. The ash layer consists of fused ash particles in a sodium sulfate matrix. The bright spots in Figure 18 are unusual; spot analyses show that the composition of these is approximately 85 wt% Fe_2O_3 with 9% TiO_2 and 4% MgO. These presumably formed by reaction of the ash with sodium sulfate, since such compositions are not present in the ash. A closer look at the surface region shows a reaction layer that corresponds to a composition of $MgO\text{-}CaO\text{-}2SiO_2$ which is approximately 30 microns thick.

Sample C.3 consisted of Wyodak ash and excess sodium sulfate on Hexoloy SA. The ash reacted with the sodium sulfate and appeared very similar to the ash in sample B.3. At the surface a thick (20 to 30 mm) layer of calcium magnesium silicate is observed. This is remarkably similar to the 30-mm thick reaction layer observed at the surface of the NT-230 siliconized silicon carbide. Just above the calcium magnesium silicate layer in sample C.3 are regions high in calcium and sulfur and high in sodium and sulfur. On top of these is the bulk ash layer which shows relatively uniform concentrations of Al, Na, and S.

The ash in sample D.3 (NT-230 substrate) appears very different from pure Illinois 6 ash as Figure 19 shows. The added sodium sulfate has reacted with the ash to form a glassy layer containing large (50 to 200 mm) bubbles. The composition of this glass is mainly a sodium aluminosilicate uniformly distributed, according to element maps. Figure 19 shows pits on the surface, indicating reaction between the ash and the silicon carbide. Such pits were also observed with the Wyodak-Na_2SO_4 (sample C.1). A few small

FIGURE 17. SEM PHOTOGRAPH OF NT-230 AFTER REACTION WITH WYODAK ASH AT 1248K

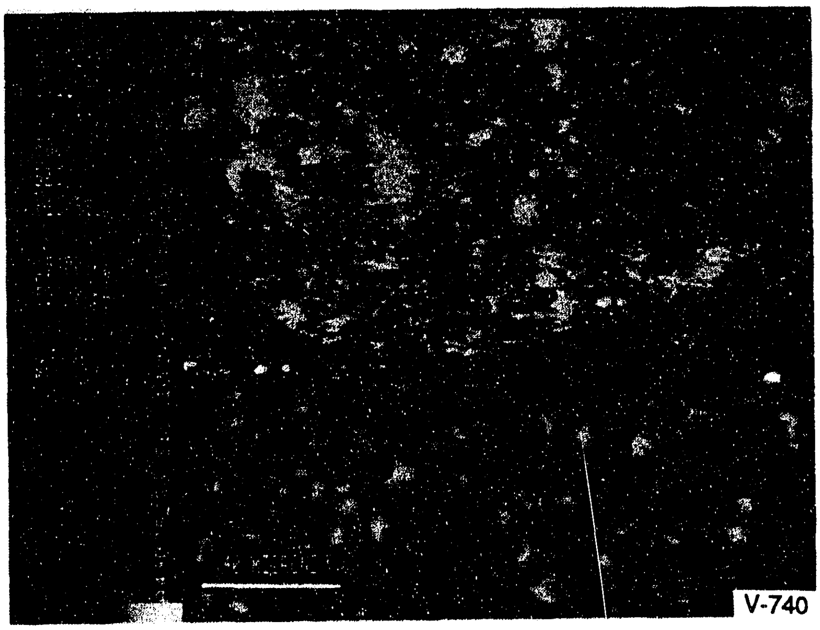

regions of sodium silicate can be seen on the surface, but, in contrast to the Wyodak-Na_2SO_4 sample, there is not a large, distinct reaction layer.

The Illinois 6 ash plus Na_2SO_4 in sample E.3 (Hexoloy SA substrate) appears the same as that in sample D.3: a glassy ash with large bubbles and uniform composition. As with the NT-230 sample, there are small regions of what may be a thin sodium silicate layer at the surface, but it does not appear to be continuous. Pitting is observed at the silicon carbide surface, as well. The pits do not appear to be as large as those observed in the NT-230 material, but it is difficult to be quantitative about the rates of reaction.

Conclusions

Based on these preliminary experiments, there are implications for interactions between silicon carbide in the air heater and condensable sodium sulfate and/or ash. It should be noted that the thick layer of sodium sulfate applied to the silicon carbide samples may not be typical of what would condense in the HITAF, although these experiments provide a "worst case". Long-term, dynamic testing under more realistic conditions will be needed in Phase II to provide quantitative rates of corrosion. However, the results of these experiments provide insight into mechanisms for corrosion and regimes of temperature that are important.

Equilibrium calculations predict that sodium sulfate should condense at temperatures below approximately 1200 K. At these temperatues, however, sodium sulfate alone (with no ash) did not react with silicon carbide. Above approximately 1300 K, sodium sulfate does not condense according to equilibrium calculations; the exact dewpoint will depend on the amount of sulfur and sodium in the coal.

In the temperatures of the experiments (1173 to 1248 K), there was only limited interaction between ash alone and silicon carbide. The most pronounced interaction was between high calcium Wyodak ash and NT-230 silicon carbide, resulting in a thin layer of calcium silicate. Such a reaction was not observed between Wyodak and Hexoloy SA silicon carbide. Illinois 6 ash did not react with either type of silicon carbide in this temperature range.

FIGURE 18. SEM PHOTOGRAPH OF NT-230 AFTER REACTION WITH WYODAK ASH AND EXCESS SODIUM SULFATE AT 1248K

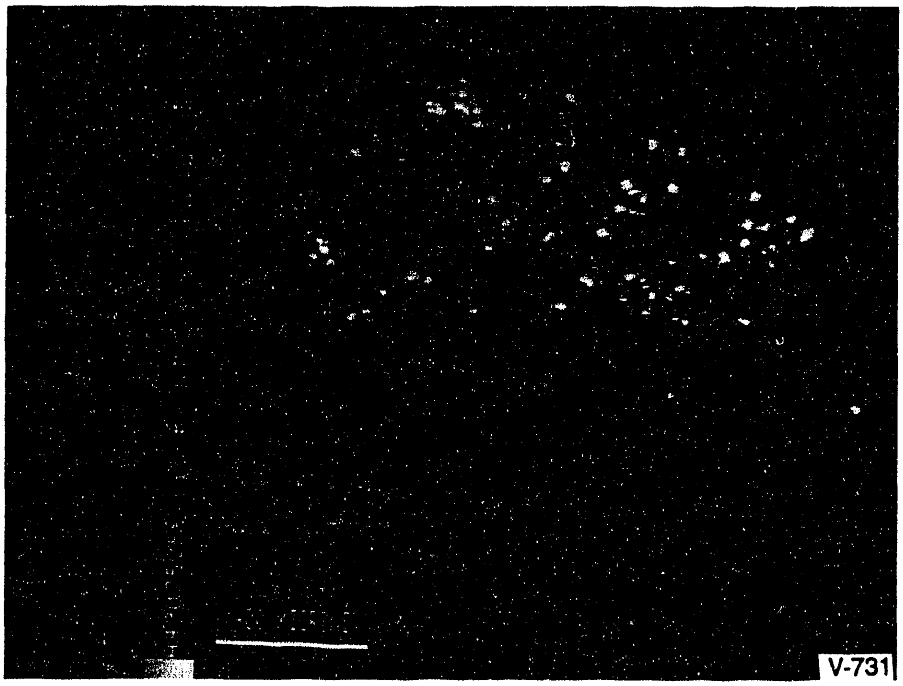

FIGURE 19. SEM PHOTOGRAPH OF NT-230 AFTER REACTION WITH ILLINOIS 6 AND EXCESS SODIUM SULFATE AT 1248K

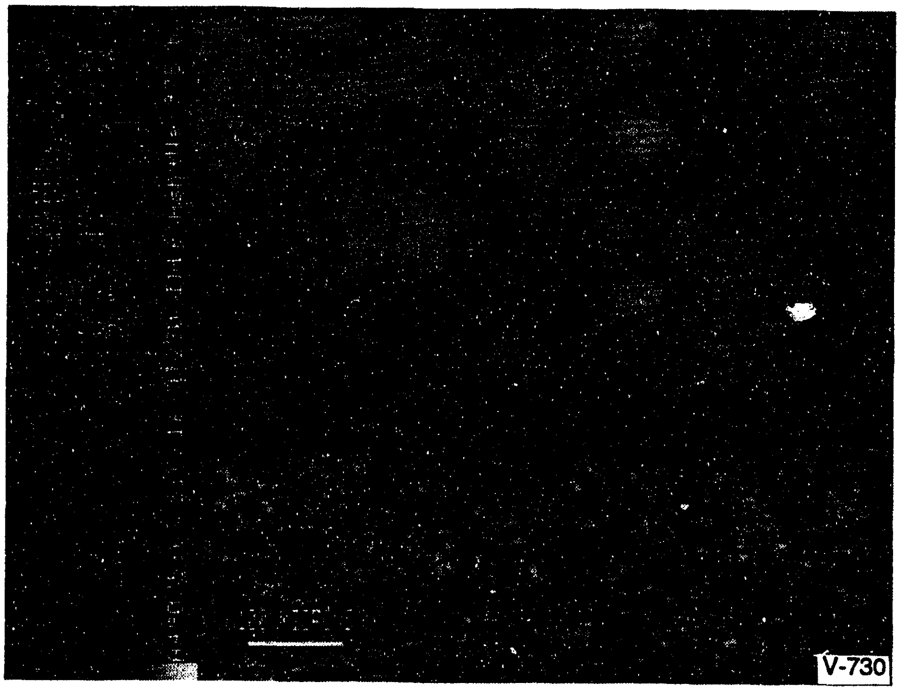

TASK 3.2.3 DEPOSIT INITIATION AND GROWTH ON CERAMIC SURFACE

Refractory Experiments

Preparations were made for the sting tests of the dense SiC materials. The sting tests will be conducted at three temperatures: 2000, 2300, and 2600F (1366, 1533, and 1700 K), using two coal ashes and four candidate structural ceramic materials. The two coal ashes selected for the experiments include a high-calcium basic ash, which was used in high-temperature experiments during the last quarter, and a high-iron coal ash, which was included in experimentation during this quarter. During this quarter, lower-temperature testing of refractory interactions with the coal ashes was initiated.

The refractories tested contained either phosphorus-based or calcium aluminate-based high-temperature binders. Other experiments during this quarter revealed that prefiring phosphorus-containing materials with nonphosphorus materials resulted in glass formation on the nonphosphorus materials. Vaporization of the phosphorus binders and subsequent deposition of phosphorus-containing phases onto other samples may have caused the extensive formation of glass foam on the surfaces of previously tested samples. Future work with these refractories will attempt to eliminate this interaction by testing phosphate-bonded materials separately. Both the phosphate and calcium aluminate binders in these materials reacted extensively at high temperatures (1700 K) with a high-calcium, basic slag in previous experiments. Several methods used to reduce the amount of binder material in the SiC refractories will be discussed in this report.

Tests at 2000F with SiC Refractories

Slag tests were performed at lower temperatures using two SiC castable refractories, Carbofrax 11LI and Harbide 80. These refractories were chosen for the experiment because they did not contain phosphorus binders, which were found to produce vesicular glass on the surfaces of the refractories. An experiment at 2000F (1366 K) for 40 hr was completed using two coal ashes: a high-calcium, basic ash (base/acid = 1.0) and a high-iron ash (base/acid = 0.4). The samples were quenched and examined using optical microscopy, scanning electron microscopy with energy dispersive x-ray analysis (SEM/EDX), and x-ray fluorescence (XRF).

The high-calcium ash was somewhat sintered, but porous and friable, after the 40-hr exposure (Figure 20). The high-iron ash was well sintered and more dense than the high-calcium ash. The ashes were attached only to the base of the refractory boats and were easily removed from the refractory. The higher coefficient of thermal expansion of both ashes, relative to the SiC refractories, allowed the ashes to shrink during cooling and detach from the walls of the refractory boats. X-ray fluorescence of the ashes after the exposure showed that they did not react with the refractory.

Tests at 2300F with SiC Refractories

A similar slag test was initiated at 2300F (1533 K) using the same castable SiC refractories, Carbofrax 11LI and Harbide 80, and the same two coal ashes. The samples were held at temperature for 45 hr, then quenched and examined using SEM/EDX. Both ashes were liquid at 2300F and did react somewhat with the refractory materials. Both samples contained a reddish reaction layer and some iron-rich phases at the refractory/slag interfaces. Figure 21 shows the high iron ash after reaction.

FIGURE 20. A PHOTO OF TWO SiC REFRACTORIES EXPOSED TO A HIGH-CALCIUM, BASIC ASH AT 2000°F (1366K)

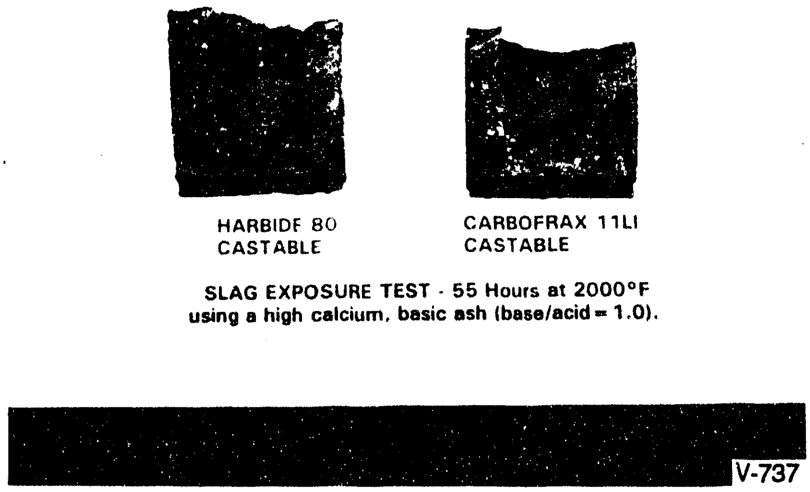

FIGURE 21. A PHOTO OF TWO SiC REFRACTORIES EXPOSED TO A HIGH-IRON ASH AT 2300°F (1533K)

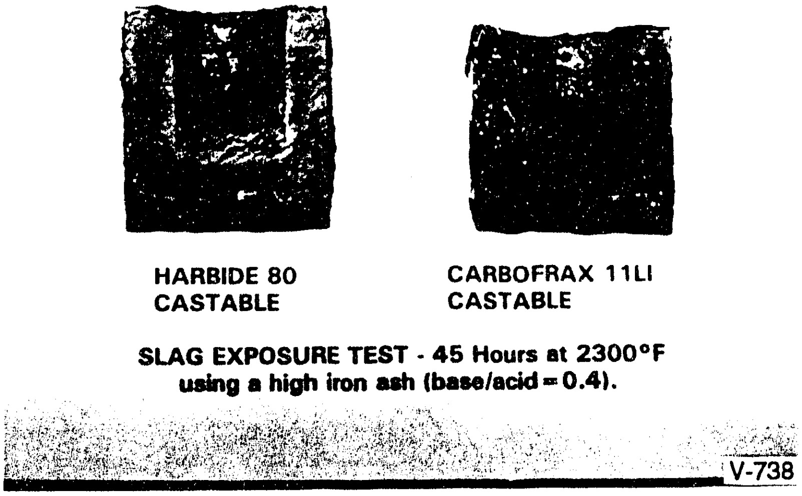

SEM/EDX analyses of the samples exposed at 2300F revealed that the high-calcium ash reacted with the refractories to produce slags with less calcium and more silica than the original ash. The high-iron ash reacted with the SiC refractories to produce slags with less iron and more silica than the original ash. Although there was some reaction between the refractories and slags at this temperature, the reactions were not as extensive as reactions at 2600F described in the October through December 1992 quarterly technical progress report.

Tests at 2600F with Non-SiC Refractories

Other refractory materials were examined for use in the Combustion 2000 sting tests. An alumina (Castable 141A) and an alumina-silica (Gun-Ram 70) castable refractory manufactured by Premier were prefired and subjected to a slag test at 2600F for over 40 hr. The Alugard 70 refractory was not included in the slag experiment because it contained a phosphate binder and had high porosity after prefiring. The Gun-Ram 70 material was also quite porous after prefiring due to the large grain sizes of this material and the absence of smaller matrix to fill the pores between grains. The alumina material did not seem to be porous after prefiring.

The refractories were quenched after 40 hr of exposure. The Gun-Ram 70 material collapsed when it was removed from the furnace; the slag had infiltrated the porous surfaces of the sample. The slag was also readily absorbed by the Castable 141A refractory, which was discolored by the slag infiltration. Because of the poor performance of these materials at this temperature, they were not examined by SEM/EDX.

Experiments with Coatings

Commercially available coatings were applied to the surfaces of the Gun-Ram 70 and the Castable 141A materials to reduce their porosity. The first coating was a zirconium oxide paint, which was also porous after drying. The coating did not prevent slag infiltration of either material. The second coating was a sodium silicate/alumina paint. This coating adhered well to the Gun-Ram 70 material, but spalled and cracked from the surface of the Castable 141A. After exposing the samples to a high-calcium coal ash for 40 hr, the coated Castable 141A sample developed two large cracks that went halfway through the sample (Figure 22). The coated Gun-Ram 70 sample was intact, but the slag was able to penetrate the coating and the refractory.

Other non-SiC materials were tested for use in the sting tests and included a chrome-alumina, phosphate-bonded mortar. The material had a chrome content of approximately 10% and was mainly composed of alumina. This material was used as a coating on the SiC, alumina, and alumina-silica refractories, which were then subjected to a 60-hr slag test using high-iron and high-calcium ashes at 2600F (1700 K).

The Carbofrax 11LI SiC and the Alfrax 66 alumina samples were analyzed using SEM/EDX to determine the interactions at the slag/chrome coating and the refractory/chrome coating interfaces for high-calcium ash. Both refractories contained some areas where the chrome coating was dissolved. These areas contained high amounts of silica and alumina with lesser amounts of phosphorous, chrome, sodium, and calcium. The Carbofrax 11LI refractory had up to 10% P_2O_5. The phosphorus in the coating material may have reacted with the binder in the SiC refractory to dissolve the chrome-alumina coating.

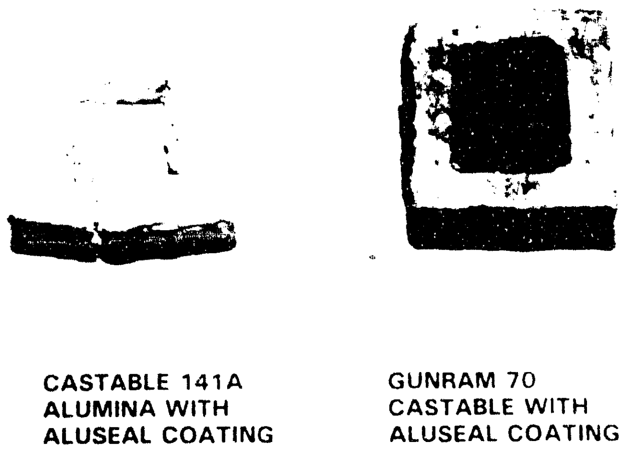

SLAG EXPOSURE TEST - 40 Hours at 2600°F
using a high calcium, basic ash (b/a = 1.0).

V-739

FIGURE 22. A photo of the alumina-silica and alumina refractories after a slag exposure experiment at 2600°F (1700 K). Both were coated with a sodium silicate/alumina paint before the exposure. Note the large crack through the sample on the left.

The Harbide 80 SiC and the Castable 141A alumina refractories were coated with the chrome material and exposed to high-iron ash.
The Harbide 80 SiC had areas where the coating was dissolved, similar to the Carbofrax 11LI sample previously described. The binder in the Castable 141A refractory did not react with the chrome-based coating, but the high-iron slag did react quite extensively with the coating. The resultant slag composition contained higher amounts of alumina and lower amounts of silica and iron than the original ash composition. Some areas of the slag contained very high amounts of chrome and alumina. The chrome-based coating did not provide an adequate barrier to either the high-calcium slag or the high-iron slag in these experiments.

Experiments with Binders

Previous testing of refractories at 2600F revealed that the binder materials reacted extensively with the slag to change the slag composition. Several methods were used to reduce the amount of binder in the SiC refractories. Two dry refractory materials (Carborundum 11LI and Harbide 80) were mixed with raw, -400-mesh SiC powder to reduce the amount of binder material in the final product. Replacement percentages ranged from 15 to 75%.

The 25 and 50% replacement materials were subjected to a slag cup test using the high-calcium ash at 1427 C for 40 hr. The samples were bonded to the furnace substrate after the exposure because the slag was able to corrode through the base of the refractory boats. The materials with replacements of raw, -400-mesh SiC were less resistant to slag attack. The corrosion could be reduced by using appropriately sized raw SiC, i.e., a well-graded material with larger particle sizes, which would reduce porosity.

Several organic binders were also tested to reduce the original amount of binder materials in the SiC refractories. Polyvinyl alcohol and polyethylene glycol were substituted into the dry SiC refractory materials, which resulted in a material with 25% original dry refractory and 75% replacement mixture (3% organic binder and 72% raw, -400-mesh SiC powder). The addition of these binders did not reduce the amount of water needed to make the mixes workable. The cured samples containing 3% of these binders did not have adequate green strength and disintegrated during handling.

Recommendations for HITAF Materials

Radiant Zone

Some of the SiC refractories contained porosity and reacted quite extensively with the high-calcium and high-iron slags at 2600F. The evidence suggests that the phosphorus-based and calcium aluminate binders in these refractories may be the cause of some of these reactions, and methods will be identified to mitigate these corrosion problems. After examination of several SiC refractories, it is recommended to utilize a material similar to the Carbofrax 11LI SiC Castable or Carbofrax 11LIG SiC Gunnable refractory manufactured by Carborundum Company, for use as a protective coating for the radiant section of the HITAF.

Some of the corrosion mechanisms of SiC by coal slag need to be better understood. In this research, it was determined that corrosion occurs in localized areas with rapid corrosion rates instead of an even surface recession. Therefore, "hot spots" may exist in the refractory lining that can be breached fairly rapidly and will need to be monitored to prevent attack of the underlying SiC air tubes. More investigation of the refractory binder interactions with the coal slags should also be pursued to determine if they play a role in this "hot spot" corrosion mechanism.

Adiabatic Zone

The most appropriate materials for the adiabatic zone of the HITAF are high-alumina, insulating refractory materials. Some materials concerns for this portion of the HITAF are the high temperatures (3000 to 3300F) and the slagging environment. Some available materials may withstand the high temperatures, but the presence of running slag may drastically reduce refractory life. Support for the structure is also not a minor detail, especially in this harsh environment. The structure must be appropriately supported, so that any dissolution or localized failure of the refractory is not followed by catastrophic failure of the entire system.

TASK 3.2.5 MODEL SLAG BEHAVIOR

In the Combustion 2000 program, we need to model the flow of a slag layer on a hot, vertical wall in order to model heat transfer through the slag. First, it is useful to discuss the critical viscosity of glasses which is necessary to understand the behavior of slag deposits. Coal slags exhibit Newtonian flow at high temperatures. There is a sharp increase in viscosity below a certain temperature. This viscosity is called the critical viscosity and the temperature is denoted by T_{cv}. The rapid increase in viscosity as the slag cools is due to formation of crystals in the liquid. The critical viscosity for coal slag is in the range of 10^2 to 10^4 poise.[7] A glass can exhibit Newtonian behavior at temperatures below T_{cv} if it is cooled so as to prevent crystal formation.

The temperature of critical viscosity is a function of composition. Hoy, et. al[8] developed a correlation for T_{cv}. Below T_{cv}, the slags are Newtonian fluids. Between T_{cv} and T_f, the solidus temperature or freezing temperature, the slags show plastic behavior. Rodgers[9] used these data to test some simplifying assumptions in his model of slag flow. The results of these calculations show that as an approximation, the temperature of critical viscosity can be taken as an effective freezing temperature. Note that in previous heat transfer calculations, we assumed that the slag freezes at T_{250}. The difference between these two temperatures is in the range of 50 to 200K. Using Tcv for the heat transfer calculation will probably more closely approximate slag flow than using T_{250}. The next level of complexity is to use a more sophisticated model of heat and mass transfer as did Rodgers. The slag layer treatment will be incorporated into the radiative heat transfer model next quarter. Results of these calculations should provide a better estimate of the effects of the slag layer on heat transfer in the radiant air heater.

TASK 3.2.6 DUCT HEATER CONCEPT SCREENING

The objective of this task is to develop the concept for an in-duct gas fired heater which will raise the air temperature from 1800F (the discharge of the air heat exchanger) to 2495F, the temperature required at the turbine inlet for the proposed cycle efficiency. This heater is to have low pressure loss and produce low levels of NO_X.

One of the principle sources of oxides of nitrogen created in combustion processes is thermal NO_X, produced principally via the Zeldovich Mechanism. Because of the strong dependence of NO production on temperature, it is important that temperatures at any point in the combustion process be kept at minimum levels conducive to the energy release required if NO_X concentrations are to be minimized. This means that the combustor should operate in a lean stoichiometry at all times and at all locations. The key to this is to provide very rapid mixing of the fuel with the oxidizer, thereby reducing local mixture inhomogeneities and limiting residence time at these less-than-optimum conditions. Rapid mixing in conventional combustors has usually required high swirl levels, and numerous fuel injectors, resulting in a high pressure loss and the resultant degradation of cycle efficiency.

Experiments have been performed at UTRC and P&W Aircraft in advanced combustors which utilize the density gradients present in swirling reacting flow to enhance mixing. This concept is called "Centrifugally-Enhanced Mixing". Results have shown that complete mixing of two streams (fuel and oxidizer) can occur in less than two swirler diameters, as long as the combustor and fuel injection module are carefully designed. With such rapid mixing, it may be possible to inject fuel (methane or natural gas) into the heated air stream with such efficiency that the stoichiometry of the fuel-air mixture can be kept very lean. This will result in low peak temperatures, and therefore low NO_X production. The advantage of this type of mixer/injector design is that experiments have shown the devices to have very low pressure drop through the combustor. The key items to be examined are the effectiveness of mixing with the injector, and the overall penetration of the fuel-air mixture into the main air flow path.

Technical Approach

To develop a low-pressure-loss, rapid mixer for the in-duct boost heater, it is most cost effective to screen preliminary concepts in a reduced scale cold flow apparatus. Efficiency of the mixer can be determined using planar digital imaging and probe sampling with the goal of minimizing pressure losses within the duct heater while maintaining a uniform mixture profile. The cycle analysis performed as part of the proposal has indicated that the density ratio of the fuel to the main air flow in the in-duct heater will be 2.35, with a duct diameter of 6 feet. In this phase of the program, it seemed most efficient to examine the centrifugally enhanced mixing concept in a 1/12 scale model of the duct heater, use air to simulate the fuel, and a mixture of air and helium to simulate the hot gas stream. These gases provide the appropriate density ratio between the injected "fuel" and the heated "air". For ease of construction and to maintain manageable gas flows in a laboratory, the duct diameter was chosen to be 6 inches, with centrifugally-enhanced mixing injectors of 1 inch diameter. A mixture of helium and air (58% by volume of helium) was used in the outer swirl passage, with air in the central core. By seeding the central air flow (representing the high density fuel in the actual duct heater) with a methane trace gas, an FID was used to probe the discharge of the swirler-injector at specific axial and radial locations in the duct to determine the concentration profile. Flow visualization was performed by seeding the central air flow with a mineral oil seed, and using Mie-scattered light intensity from an

FIGURE 23. METHANE DUCT BURNER

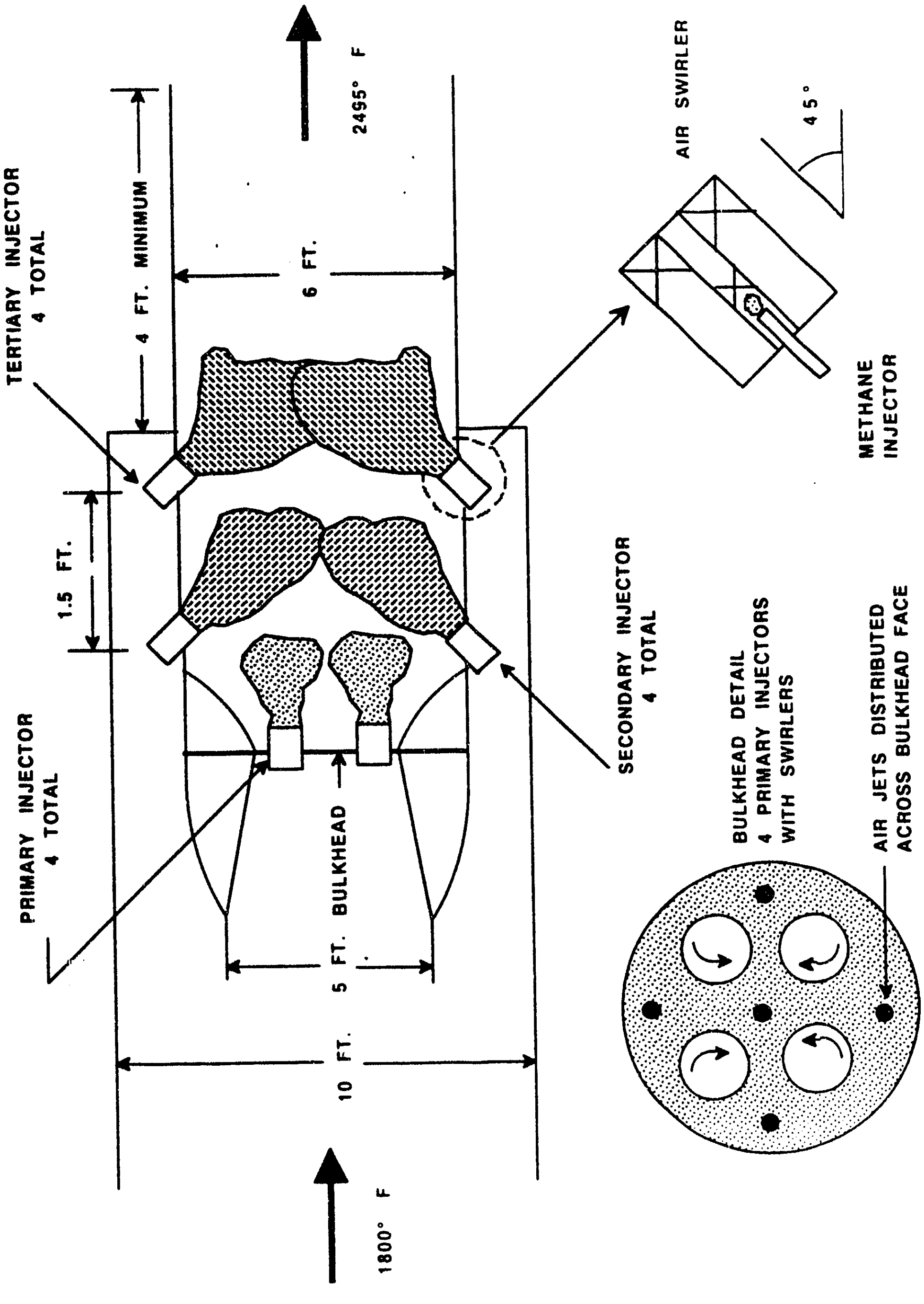

argon-ion laser to determine relative concentration of the seeded gas in the duct. Results from each of these investigations are discussed below.

Flow Visualization

The duct heater concept originally proposed utilizes an array of centrifugally enhanced mixers arranged in stages around the circumference of the duct as shown in Figure 23. The concept was based upon using the penetration of the individual jets into the main stream to provide a uniform exit temperature profile, while obtaining rapid mixing in each injector using the centrifugal mixing concept. To evaluate the mixing profile for an individual injector, tests were performed in a rectangular duct using planar digital imaging to determine concentration profiles of injected gas into the main flow. The jet flow was marked with mineral oil seed which was illuminated by sheets of light formed by an argon-ion laser and a rotating mirror system. The resultant image was captured and digitized by a CCD camera and associated data acquisition equipment. By normalizing the intensity of the image at any point in the duct with the intensity at the discharge of the jet into the duct, the relative concentration of jet fluid in the main flow can be determined. A conceptual representation of this apparatus is shown in Figure 24.

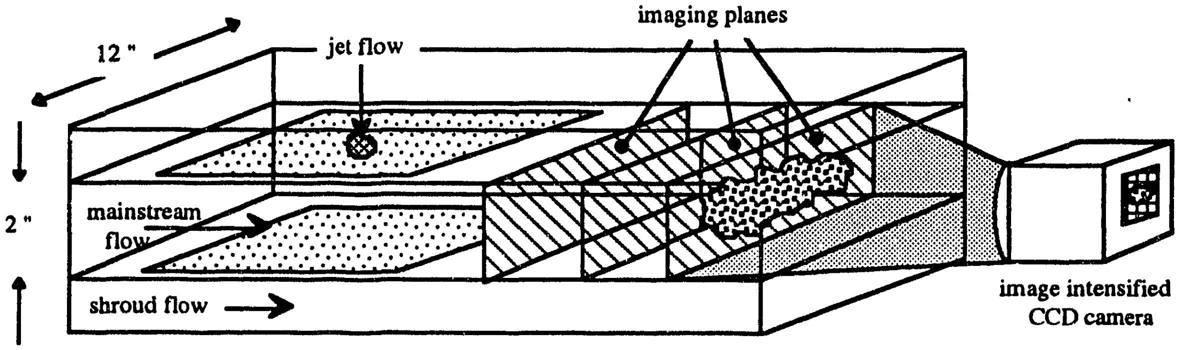

Figure 24. Flow Visualization Apparatus

The main duct velocity as proposed was approximately 50 feet/sec, with each of the 12 injectors introducing 30.27 lbm/sec of air at a velocity of 195 feet/sec and 0.302 lbm/sec of fuel at a velocity of 87 feet/sec. Using the target velocity ratios, the sub scale experiment in injector mixing was operated at a main flow velocity of 4 feet/sec in order to provide a flow field that could be imaged properly and ensuring that the marker particles would faithfully follow the flow. Although this experiment was approximately 1/12 scale, the momentum ratios were maintained as close as possible to that which would be expected in the full scale apparatus. As has been previously demonstrated, the momentum ratio is a critical parameter in cross-stream jet mixing if the jet diameter is normalized by duct height in analyses. The mainstream flow was constant, and imaging was performed at several locations downstream of the injector location for several velocity ratios in order to explore the effect of velocity on the jet penetration. The injector consisted of a double swirl module of 0.87 inch diameter with 45 swirl vanes in the center and annular flows, similar to the proposed full scale device. The swirlers were designed and manufactured using stereo lithography and CAD techniques which could be used to optimize the swirler design for pressure drop and flow characteristics.

The results of the flow visualization experiments can be dramatically seen in Figure 25 showing a plane located just downstream of the swirler exit plane. The view is as shown in Figure 26, with the plane transverse to the main flow and the camera looking upstream. The significance of these images is that it demonstrates that the centrifugal mixer works too well to provide adequate penetration of the jet into the main flow. From the concentration contours, represented by a false color image, it is evident that the swirler flow spreads radially along the wall, indicating very rapid transverse mixing, but the majority of the gas does not penetrate into the main flow. This would result in very poor temperature profiles in the duct heater and probably areas of high NO production. The heater exit pattern factor, defined as the deviation of local temperature from the average temperature, normalized by the average, would be large and would therefore present problems for the turbine inlet guide vanes and first stage rotor due to large thermal variations and accompanying stresses.

Mixer Concentration Measurements

Based upon the flow visualization results, a new duct heater concept was developed. This concept, shown in Figure 26, consists of 12 centrifugally-enhanced mixers distributed in equal area sectors across the duct. Each injector will handle the same flows as listed above, and will be responsible for the fuel and air flow for each sector of 2.356 square feet area.

It was apparent that the centrifugal mixer provides very rapid transverse mixing at the velocity and density ratios to be found in the duct heater, so this characteristic was used to an advantage in designing the duct heater concept shown in Figure 26. To study the mixing in more detail, an experimental apparatus was built to perform probe sampling of the flow in both the near and far field of the mixer-injector. To accomplish this, the swirl module was designed with air flowing in the center passage (shown in Figure 27), and a mixture of air and helium flowing in the outer passage as described above. Based upon chemical kinetics studies using the CHEMKIN© computer code, the temperature rise needed in the duct heater is predicted to require an overall stoichiometry of 0.187, which calculates to a fuel mole fraction of 0.018. The more rapidly the mixer-injector can achieve this fuel mole fraction, the shorter the residence time at higher stoichiometries. Therefore the thermal NO_X can be minimized. The sub scale test apparatus was designed with critical flow orifices or laminar flow elements used to meter the flows in each passage so that each gas flow could be measured accurately. The inner flow was seeded with methane tracer so that there was sufficient concentration at the discharge to measure with confidence while constantly monitoring the seed concentration to ensure it was stable. Typically, the inner air was seeded with 800 ppm of methane, with concentrations of 14 ppm measured when the flow was completely mixed. Once again, several flow velocity ratios were tested, with one being the anticipated ratio to be used in the full scale device. The density ratio was determined by the fuel-air density ratio in the actual duct heater.

The results of these gas composition experiments is shown for the expected density and velocity ratios in Figure 28. This figure shows radial composition profiles at 5 axial positions using a 0.0625 inch diameter sampling probe. The O.D. of the inner flow passage was 0.87 inches. From the figure, the data indicates that the inner and outer flows are completely mixed in 1.1 swirler diameters downstream of the swirler exit plane. Tests were also performed at various mass flows through the swirl module to determine the affective C_DA for the swirl module design. A larger diameter swirler (1.875 inch O.D.) was also tested to examine scaling effects. From the air flow data, the pressure drop that can be expected in the full scale device under the operating conditions listed in the proposal will be 1.3%, which is within the target of 1.5% total pressure drop.

FIGURE 25

FLOW VISUALIZATION OF DUCT HEATER INJECTOR
TRANSVERSE INJECTION IN COLD FLOW TEST

VELOCITY OF MAIN STREAM = 5 FEET/SEC
VELOCITY OF INJECTOR STREAM = 30 FEET/SEC

CONCENTRATION OF INJECTOR STREAM REPRESENTED
BY FALSE COLOR IMAGE. RED = 100% INJECTOR FLUID

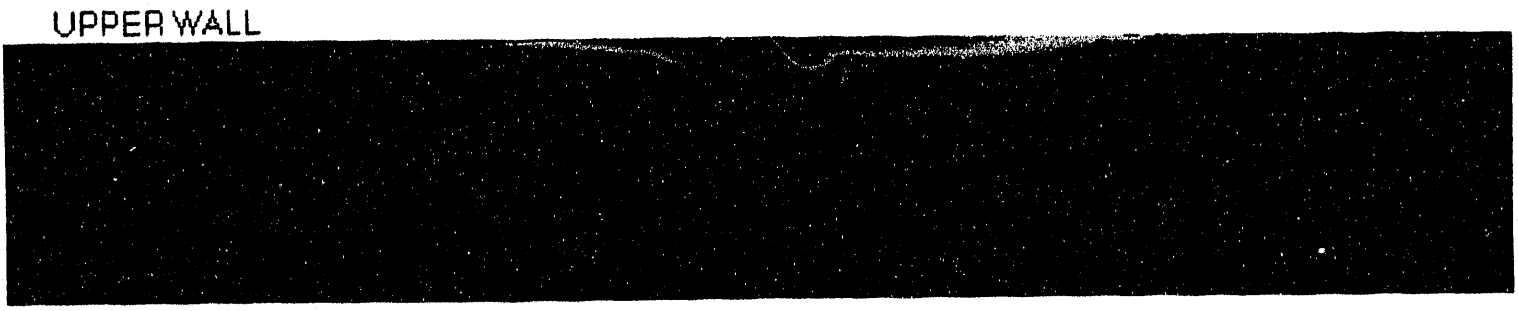

IMAGE PLANE THROUGH SWIRLER MIDPOINT

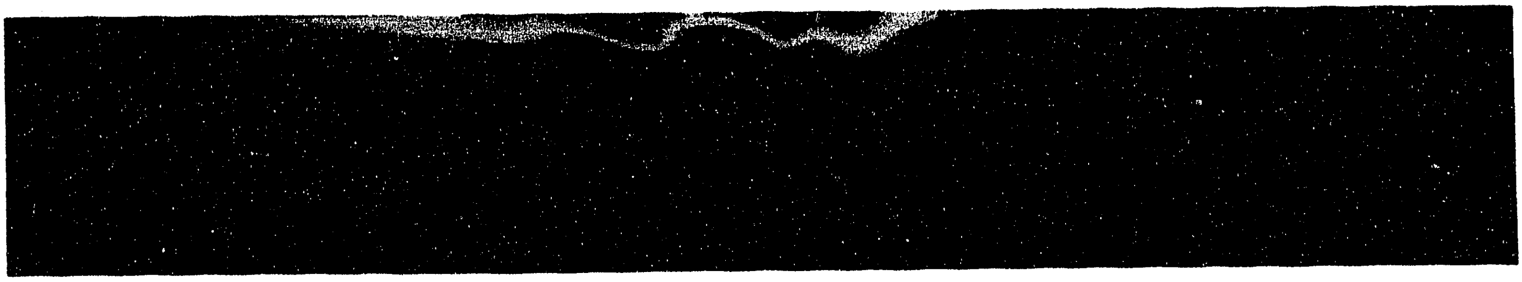

IMAGE PLANE THROUGH SWIRLER TRAILING EDGE

FIGURE 26.

LOW EMISSIONS IN-DUCT BOOST HEATER CROSS SECTION

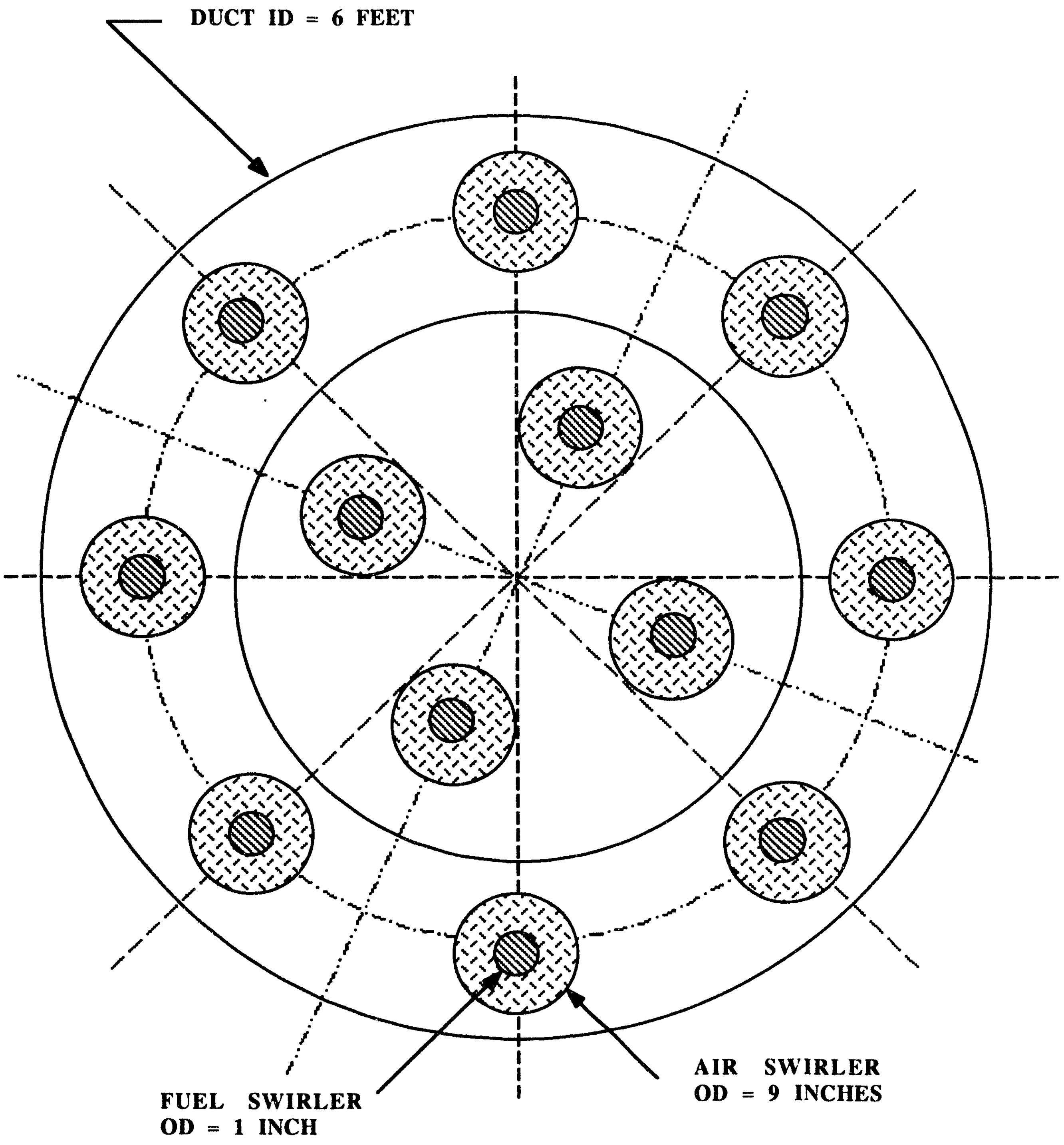

DUCT AREA = 28.27 SQ. FT.   SWIRL MODULE SECTOR AREA = 2.356 SQ. FT.

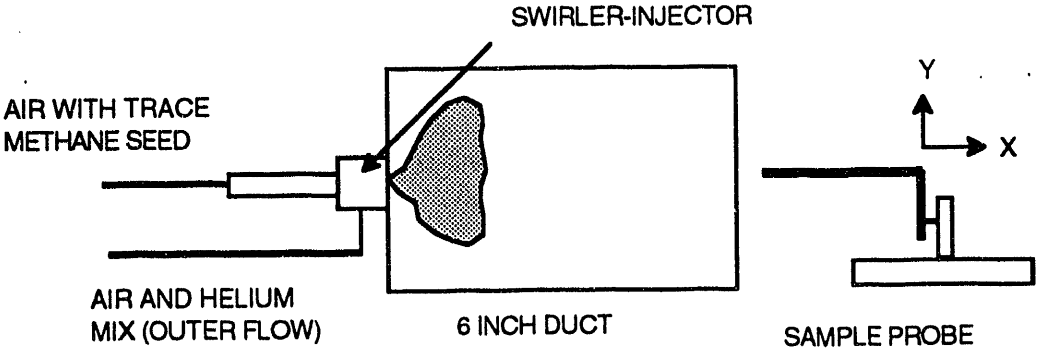

Figure 27. Schematic of Gas Composition Apparatus

Conclusions

The centrifugally-enhanced mixer concept will provide very rapid mixing of the fuel and air in the duct heater based upon projected mass flows and density ratios. The sub scale model has demonstrated the viability of the concept. From these experiments, it has been determined that transverse injection of the fuel and air into the duct will not provide adequate penetration of the fuel-air mixture into the main stream and will therefore not provide a uniform exit temperature and composition profile. With a distributed array of coaxial mixers, the centrifugally-enhanced mixer-injector concept will provide complete mixing within 1.5 mixer diameters. This rapid mixing should keep the production of thermal NO_X at a minimum. Preliminary sub scale pressure drop measurements indicate that the total pressure drop through the mixer will be 1.3%, which meets the program goal.

FIGURE 28.

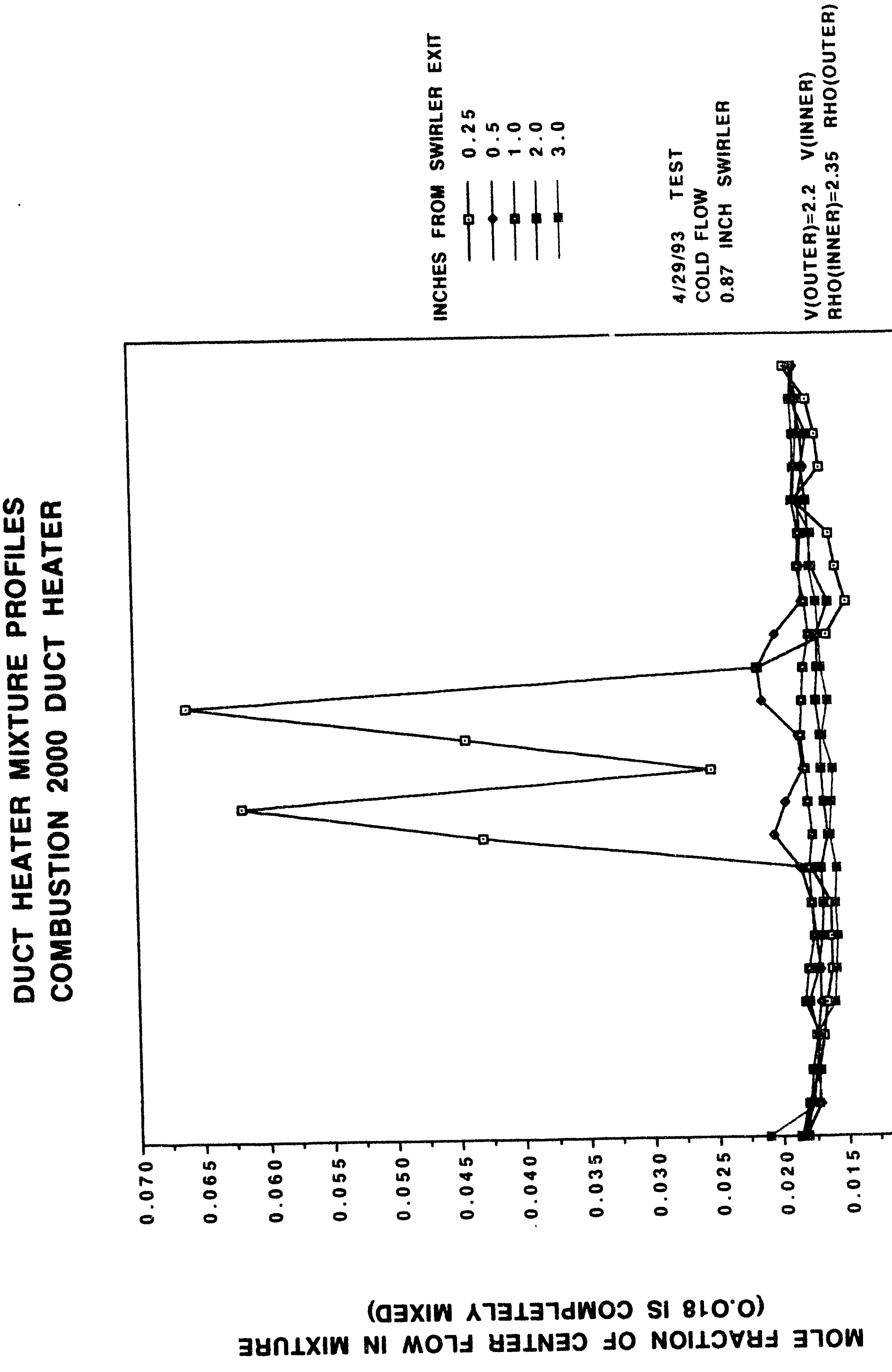
DUCT HEATER MIXTURE PROFILES
COMBUSTION 2000 DUCT HEATER
INCHES FROM SWIRLER EXIT
0.25
0.5
1.0
2.0
3.0
4/29/93 TEST
COLD FLOW
0.87 INCH SWIRLER
V(OUTER)=2.2 V(INNER)
RHO(INNER)=2.35 RHO(OUTER)
MOLE FRACTION OF CENTER FLOW IN MIXTURE
(0.018 IS COMPLETELY MIXED)
0.070
0.065
0.060
0.055
0.050
0.045
0.040
0.035
0.030
0.025
0.020
0.015
0.010
RADIAL POSITION - INCHES (0 = RIGHT WALL)
0.0
0.5
1.0
1.5
2.0
2.5
3.0
3.5
4.0
4.5
5.0
5.5
6.0

APPENDIX

COMMERCIAL PLANT DESIGN

DESIGN CRITERIA

The reference commercial power plant will consist of a single modern gas turbine and a Rankine cycle-based steam bottoming turbine. For plant design and performance definition purposes it is assumed that the gas turbine will be a V84.4 model. At ISO conditions, the gross generating capacity of this combined cycle plant is approximately 308 MWe. A process block diagram is presented in the figure at the end of the Appendix.

Site Location and Conditions

The nominal plant location and site-specific conditions are as follows:

Site-related:

- Plant site	Central USA
- Site elevation (above mean seal level) - ft	600
- Seismic zone	1
- Plant access road - mi	1
- Plant rail - mi	2
- Water transportation	Lake Michigan
- Water makeup source	Lake Michigan
- Electric power source for startup	power grid (1 mi line required)

* Representative analysis is shown in Table 1.

Meteorological

- Average annual conditions		
dry bulb temperature	F	60
wet bulb temperature	F	52
atmospheric pressure	psia	14.4
rainfall	in/y	31
- Other meteorological data		
max. dry bulb temperature	F	95
max. wet bulk temperature	F	75
minimum temperature	F	20 for performance
minimum temperature	F	-20 for freeze protection

Plant Performance Criteria

Service conditions: The plant is to be designed for base load operation, with capability to stable operation to 33 percent of design load continuously, and at 105 percent of design load (valves wide open condition) for limited time periods.

Design life: The nominal design life is 30 years.

Target efficiency: the net efficiency of the reference commercial plant is to be 47 percent or higher (minimum heat rate 7260 Btu/kWh, HHV) at ISO conditions.
Design basis fuels: The plant is to burn Illinois #6 bituminous coal as the primary fuel. The capability to operate with other coals is to be included. With other coals the power output and efficiency criteria need not be met. Composition and properties of the design coal are listed in Table 2.

Natural gas is to serve as auxiliary and warm-up fuel. Natural gas may provide up to 35 percent of the energy requirements at the design point. Composition and properties of natural gas are listed in Table 3.

Environmental criteria: Atmospheric emissions are to be limited to the following:

S02	0.15 lb/MMBtu
NOx	0.15 lb/MMBtu
Particulates	0.0075 lb/MMBtu

Liquid discharges are to be treated to meet NPDES requirements.

Solid wastes (ash and FGD sludges) are to be stabilized and shipped for off-site disposal.

ECONOMIC CRITERIA

Capital cost estimating bases:

Capital cost estimating bases: Factored estimate, corresponding to Class II estimate, as defined in 1989 EPRI TAG(TM), expressed in January 1993 dollars.

Target cost: Cost of electricity from a power plant, using fully developed HIPPS technology, to be 10 percent lower than that from an equal capacity conventional pulverized coal-fired power plant with FGD.

Projected fuel costs: The delivered cost of coal in 2010 is 1.65 $/MMBtu. For the same time, the cost of natural gas is 5.38 $/MMBtu.

Economic analysis: Constant dollar, levelized cost analysis methods will be used, assuming a startup date of January 2010. The costs are discounted to January, 1993.

PLANT DESIGN

A preliminary process block diagram was prepared, reflecting the current configuration of the major plant processes. This diagram, shown in Figure 1, is currently undergoing review by the program participants. The stream numbers, indicated on this diagram, represent the state points for which mass and energy balance information will be provided.

Layout efforts to arrange major components of the power block was initiated. The objective of this effort is to establish relative locations of components to satisfy functional requirement, minimize duct and pipe lengths, and to allow sufficient access for maintenance activities.

It is expected that the commercial power plant will require significant lengths of hot gas ducting. Design concepts and representative costs ($/ft of duct) are being developed for three duct types:

- Externally insulated warm (about 700F) duct to carry GT compressor discharge air

- Internally insulated hot (about 1 800F) duct to carry heated air from the radiant heater

- Concentric duct. The inner duct is internally insulated and carries the heated air. The outer duct, externally insulated, carries the warm compressor discharge. This duct will be used in the vicinity of the gas turbine.

The ducts are designed for 250 psi internal pressure and are sized for about 60 ft/sec air velocity. The insulation is designed to limit the external skin temperature to 140F.

Table 1. REPRESENTATIVE WATER ANALYSIS

	mg/l	mg/l as $CaCO_3$
SiO_2	6.8	--
Ca	76.0	189.0
Mg	16.0	68.0
Na	20.0	44.0
K	2.9	3.7
HCO_3	246.0	202.0
SO	56.0	58.0
Cl	26.0	37.0
NO_3	6.9	5.6
Total dissolved solids	457.0	--
Total hardness	--	255.0
pH	8.0	
Temperature range (F)	40-80	

Table 2. PROPERTIES OF DESIGN COAL

	Average	Range
Proximate analysis (% wt)		
moisture	12.0	10-14
volatile matter	33.0	31-35
fixed carbon	39.0	37-41
ash	6.0	13-19
Higher heating value (Btu/lb)	11,100	9,800-10,400
Grindability index (Hardgrove)	56	
Ultimate analysis (% wt)		
moisture	12.0	10-14
C	57.5	
H_2	3.7	
N_2	0.9	
Cl	0.1	
S	4.0	3.4-4.6
O_2	5.8	
Ash	16	13-19
Ash analysis (% wt)		
SiO_2	45	
Fe_2O_3	20	
Al_2O_3	18	
TiO_2	1	
CaO	7	
MgO		
SO_3	3.5	
K_2O	1.9	
Na_2O	0.6	0.4-1.5
P_2O_5	0.2	
Undetermined	1.8	
TOTAL	100	
	Reducing	Oxidizing
Ash fusion temperature (F)		
Initial deformation	1,950	2,250
Softening (H=Q)	2,030	2,300
Fluid	2,150	2,450

Table 3. COMPOSITION OF NATURAL GAS

Ultimate analysis (% wt)	
H_2	69.26
C	22.68
N_2	8.06
Composition (mole %)	
CH_4	90
C_2H_6	5
H_2S	0.0004
N_2	balance
Average molecular weight	17.3
Higher heating value	
Btu/scf	1,000
Btu/lb	21,824

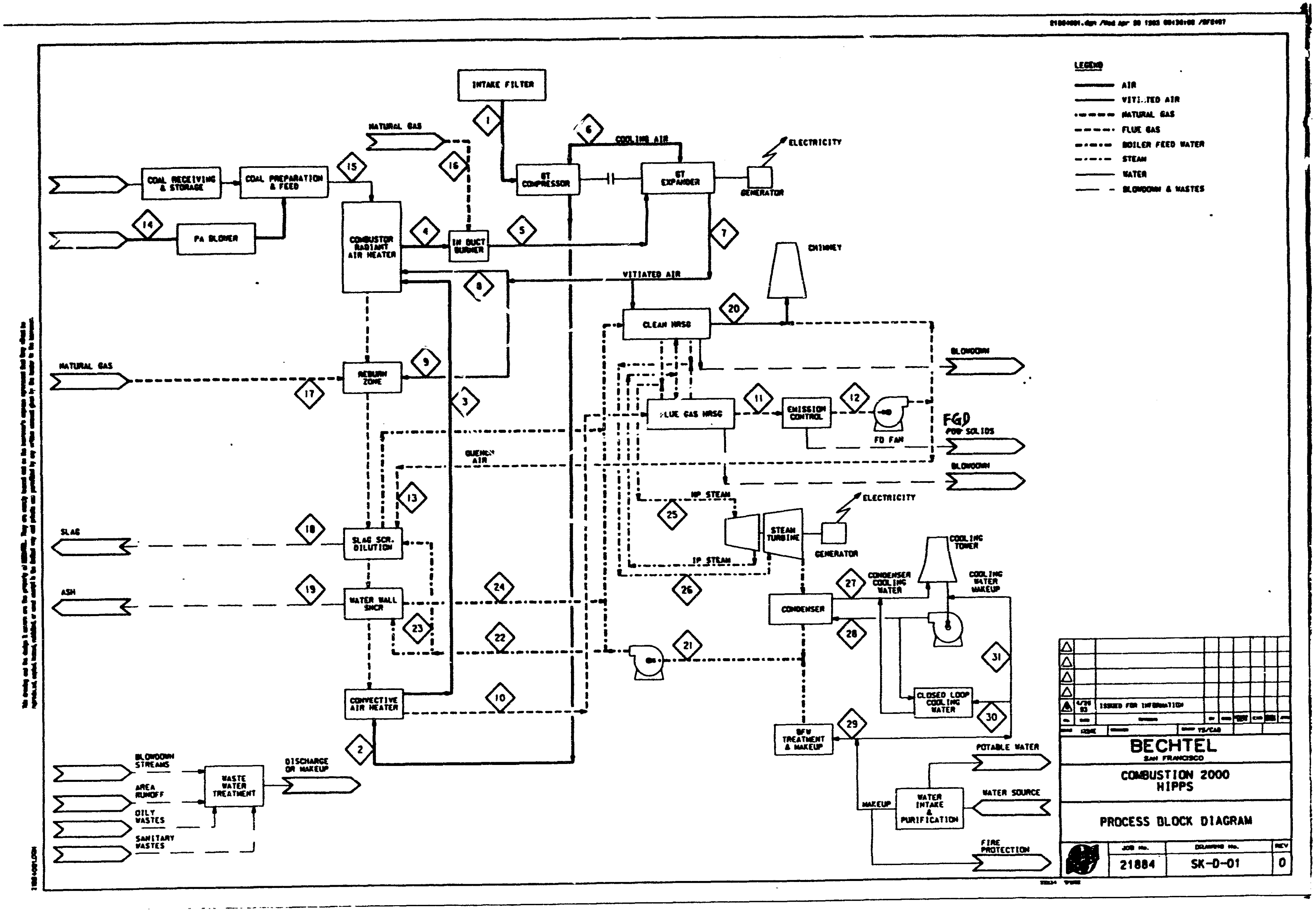
LEGEND
AIR
VITIATED AIR
NATURAL GAS
FLUE GAS
BOILER FEED WATER
STEAM
WATER
BLOWDOWN & WASTES
INTAKE FILTER
GT COMPRESSOR
GT EXPANDER
COOLING AIR
GENERATOR
ELECTRICITY
NATURAL GAS
COAL RECEIVING & STORAGE
COAL PREPARATION & FEED
PA BLOWER
COMBUSTOR RADIANT AIR HEATER
IN DUCT BURNER
VITIATED AIR
CHIMNEY
CLEAN HRSG
FLUE GAS HRSG
EMISSION CONTROL
FD FAN
BLOWDOWN
FGD
FGD SOLIDS
BLOWDOWN
REBURN ZONE
QUENCH AIR
HP STEAM
IP STEAM
STEAM TURBINE
GENERATOR
ELECTRICITY
SLAG SCR. DILUTION
WATER WALL SNCR
CONVECTIVE AIR HEATER
SLAG
ASH
CONDENSER
CONDENSER COOLING WATER
COOLING TOWER
COOLING WATER MAKEUP
CLOSED LOOP COOLING WATER
BFW TREATMENT & MAKEUP
POTABLE WATER
WATER SOURCE
WATER INTAKE & PURIFICATION
MAKEUP
FIRE PROTECTION
BLOWDOWN STREAMS
AREA RUNOFF
OILY WASTES
SANITARY WASTES
WASTE WATER TREATMENT
DISCHARGE OR MAKEUP
1
2
3
4
5
6
7
8
9
10
11
12
13
14
15
16
17
18
19
20
21
22
23
24
25
26
27
28
29
30
31
4/26 93
ISSUED FOR INFORMATION
YS/CAD
BECHTEL
SAN FRANCISCO
COMBUSTION 2000
HIPPS
PROCESS BLOCK DIAGRAM
JOB No.
21884
DRAWING No.
SK-D-01
REV
0

END

DATE
FILMED

10/25/93